Non-equilibrium dynamics of driven individual particles and 3D nano printing across scales

by

Cecelia Namuli Mweka

November, 2024

A thesis submitted to the
Graduate School
of the
Institute of Science and Technology Austria
in partial fulfillment of the requirements
for the degree of
Master of Science

Committee in charge:
Scott Russell Waitukaitis, Supervisor
Jérémie Palacci, Supervisor

The thesis of Cecelia Namuli Mweka, titled ***Non-equilibrium dynamics of driven individual particles and 3D nano printing across scales,*** is approved by:

Supervisor: Scott Russell Waitukaitis, ISTA, Klosterneuburg, Austria

Signature: _____

Supervisor: Jérémie Palacci, ISTA, Klosterneuburg, Austria

Signature: _____

Signed page is on file

ISTA Master's Thesis, ISSN: 2791-4585

I hereby declare that this thesis is my own work and that it does not contain other people's work without this being so stated; this thesis does not contain my previous work without this being stated, and the bibliography contains all the literature that I used in writing the dissertation.

I accept full responsibility for the content and factual accuracy of this work, including the data and their analysis and presentation, and the text and citation of other work.

I declare that this is a true copy of my thesis, including any final revisions, as approved by my thesis committee, and that this thesis has not been submitted for a higher degree to any other university or institution.

I certify that any republication of materials presented in this thesis has been approved by the relevant publishers and co-authors.

Signature: _____

Cecelia Namuli Mweka

November, 2024

Signed page is on file

Abstract

This thesis is an experimental work about two distinct research projects that evolved from a single project: non-equilibrium dynamics of an acoustically vibrated particle and microfabrication of particles with nano-scale 3D printing. The first project explores non equilibrium dynamics of a particle driven by ultrasonic vibrations. We design an experimental system consisting of an electromechanical vibration scheme to drive the particle's vibrations and an imaging scheme to track its trajectories. We study the trajectories to determine how the particle's dynamics evolve under the driven conditions, considering out of equilibrium systems in the context of equilibrium statistical mechanics. Using a Langevin framework and the Boltzmann factor, we characterize the particle's dynamics as complex; the particle motion is not purely diffusive. We extract physical parameters like spring constant, effective temperature, damping coefficient and resonance frequency.

In the second project, we explore and develop techniques in the design and microfabrication of particles across scales. Microfabrication involves building structures at the micron or submicron scale. These designed miniaturized patterns, objects, or devices are useful in biophysics, pharmacology, medical biology, and nanotechnology. We specifically apply two-photon polymerization, a form of 3D nano printing. We print millimetric particles, characterizing different designs to evaluate and showcase the resolution, aspect ratio integrity and print quality of the printing process. We also design and fabricate a microsensor to deflect under applicable force of order 0.1 pN. We present fundamental concepts needed to design the microsensor, showcasing 3D printing at considerably smaller scales down to the μm or below.

Acknowledgments

I would like to acknowledge Scott Waitukaitis and Jérémie Palacci, for their supervision, and their extensive support of my learning.

For the beautiful characterization images used in this work, I would like to thank Dr. Daniel Grober, Samuel Hajek and Felix Pertl.

The Palacci group, particularly Malina Strugaru and Dan Grober, for their continuous guidance in decoding and following my streams of thought.

To the Waitukaitis group, for helping me find my footing in science, and making me feel at home.

To the Nanofabrication Facility (NFF) at ISTA, for training me in significant aspects of my research. The MIBA Facility, and particularly Todor Asenov for consistently picking up the phone for my machining and designing needs.

To my friends, Mariana, Lenka, Aaron, Rebecca, Eavan who provided an ear, wine, and a lot more when I needed to vent, talk through my crises as well as experiment. For the walks, for the coffees, for reading through my work and providing edits, for dinners to take me out of blocks and binds and for cheering me on when it felt insurmountable. Finally, I am grateful to Griff and Fletcher, whose music helped me through several blocks, especially with my writing.

My science would not have been possible without the guidance, support and contributions of all these people, and more.

About the Author

Cecelia Namuli Mweka completed a BA in Physics with an emphasis on Chemistry/ Material Science at Colorado College, USA before joining ISTA in June 2021. She worked as an intern with the Waitukaitis group on the research project 'Next-gen charge measurements using acoustic levitation'. Her main research interests include acoustic levitation, 3D nanofabrication and vibration controlled statistical mechanics. In her time at ISTA, Cecelia has presented her work on charge measurements at the Electrostatics Society of America.

Table of Contents

List of Figures

List of Tables

Preamble

This thesis is about two distinct research projects that evolved from a single project: non-equilibrium dynamics of an acoustically vibrated particle and microfabrication of particles with nano-scale 3D printing. The first part focuses on the study of non-equilibrium dynamics based on trajectories, exploring how a single particle behaves under driven conditions and whether this behavior obeys the physics of the statistical mechanics of a non-equilibrium system. In the second part, we explore the design and microfabrication of particles across scales. We apply a specific method of microfabrication and the potential functionality of microfabricated structures.

At the outset of this work, the goal was fabricating custom designed structures, functionalizing them and observing their dynamics in a driven non-equilibrium system. This was motivated by work by Dauchot et al [1], where they explore experiments conducted on vibrated disks with a built-in polar asymmetry. For further novelty, we considered applying an electric field as an additional source of external force on the particles, necessitating the functionalization of printed microstructures as conductive. However, the initial experimental set up led to some interesting results, redirecting the project towards simply answering the question of non-equilibrium dynamics of a single driven particle.

The second project focuses on microfabrication across scales, ranging from the macroscale (1000 μm) to the microscale (2 μm). We also explore the feasibility of applying these microstructures in real life applications, for instance a colloidal force sensor. Additionally, this section also delves further into the processing of microfabricated structures using electroless plating.

Chapter 1 details non-equilibrium dynamics, with sections describing the experimental design, the developed toolbox of techniques used to study the single particle system, characterization results, analyses and findings related to the single particle system. Chapter 2 details microfabrication, specifically three-dimensional (3D) nanofabrication using two-photon polymerization (2PP) and the functionalization of printed structures using electroless plating. Consequent sections in Chapter 2 detail the methods, mechanisms and results of particle fabrication and functionalization, particularly the design and fabrication of a colloidal force sensor.

1 Non-Equilibrium dynamics of an ultrasonically vibrated particle

1.1 Introduction

Non equilibrium dynamics describe systems not in thermal equilibrium, where state variables like pressure, temperature or particle number are temporally inhomogeneous. Different systems that exhibit non-equilibrium dynamics include driven dissipative systems and active matter systems. Driven dissipative systems are kept out of equilibrium through continuous 'macroscale' energy input and dissipation, which results in steady states that are dynamically maintained. For example, granular materials subject to mechanical agitation [2] and turbulent fluids driven by external forces exhibit spontaneous pattern formation despite being out of equilibrium. In these systems, emergent behaviors such as clustering and phase separation have been observed [3], challenging classical thermodynamic principles.

Active matter systems operate far from equilibrium because their *individual components* consume energy to perform mechanical work. Hence, while driven-dissipative systems inject energy at the macroscale, active matter systems inject it 'locally.' In recent years, active matter systems have been proposed to include vibrating granular materials [2] [3], a droplet on a vibrating liquid interface [4], and aggregating bacterial baths [5]. The collective behavior of the individual units in the system displays some interesting emergent behaviors, such as swarming [2] [3], clustering and phase separation.

To analyze non-equilibrium systems at the particle level, statistical mechanics provides a natural reference point. This is due to the general interest in understanding what fundamental results from statistical mechanics 'survive' in systems that are not strictly in equilibrium. For instance, the Langevin equation, originally developed to describe Brownian motion, incorporates deterministic forces and random thermal fluctuations, allowing for a stochastic description of particle dynamics. While classical Brownian motion pertains to equilibrium systems, the Langevin framework has been extended to describe driven-dissipative systems. Hence, by considering out of equilibrium systems in the context of equilibrium statistical mechanics, we push the boundaries of understanding regarding their applicability.

In this chapter, we explore a single particle driven dissipative system and probe whether or not its dynamics obeys basic results in statistical mechanics. For instance, does it have a distribution among microstates set by the Boltzmann equation? Do the dynamics agree with the Langevin equation? By analyzing particle trajectories in non-equilibrium systems, we aim to deepen our understanding of how external driving forces and internal fluctuations influence system behavior at both microscopic and macroscopic scales.

1.1.1 Theoretical framework

1.1.1.1 The Langevin equation

Classically, Brownian motion of a single particle can be treated analytically using the Langevin equation, which describes the velocity of a particle evolving through time as a function of both random and systematic forces. In this particular system, a single particle of mass, m, velocity, v where the systematic force is a spring-like force as a result of the system's geometry, kx, and a time dependent random force $\eta(t)$ due to the acoustic vibrations in the system, the Langevin equation is:

$$m\frac{d\mathbf{v}}{dt} = -\gamma\mathbf{v} - kx + \eta(t) \tag{1.1.1}$$

Following Uhlenbeck and Ornstein [6], Chandrasekhar [7], Wang and Uhlenbeck [8], it is assumed that the random force satisfies the conditions that (a) its strength is Gaussian distributed, and (b) that its correlation time is infinitely short. This forms the basis for the analysis of a particle's trajectory over time.

1.1.1.2 The Boltzmann factor

The Boltzmann factor corresponds to a system in thermal equilibrium, with temperature T, and yields the probability, $P(E)$, that the system will have energy E [9]. The distribution of these probabilities is proportional to the number of accessible states and is described as:

$$P(E) \propto e^{-\frac{E}{k_B T}}, \tag{1.1.2}$$

where k_B is the Boltzmann constant, and T the absolute temperature, linking the macroscopic thermal properties of the system to the microscopic statistical distribution of the energy states. The decaying exponential form of the Boltzmann factor indicates that higher energy states are exponentially less likely to be occupied as the energy increases.

To derive the relevant equations describing the probability of velocity and position as a function of energy distribution, we assume a system in contact with a heat reservoir. The probability that the system has energy E is given by the ratio of the number of the microstates associated with that energy to the total number of microstates in the system. By normalizing this distribution, we arrive at the full expression for the probability:

$$P(E) = \frac{e^{-\frac{E}{k_B T}}}{Z} \tag{1.1.3}$$

where Z is the partition function, a sum over all possible energy states E_i:

$$Z = \sum e^{-\frac{E_i}{k_B T}} \tag{1.1.4}$$

To extract the positional distribution and the velocity distribution as a function of the energy in the system, we consider the Langevin equation presented in 1.1.1.1. A complete derivation of the expressions describing the position distribution and the velocity distribution as a function of the Boltzmann factor are presented in Appendix B and Appendix C.

1.1.1.3 **Power Spectral Density**

Derived from the Langevin equation and the simple harmonic oscillator relationship as described in Appendix D, the Power Spectral Density (PSD) provides information on the distribution of power across the frequencies represented in the system. This accounts for the systematic and random forces acting on a particle. By applying Fourier transforms, we analyze the frequency domain where the power associated with each frequency is extracted. The resulting PSD gives a frequency-dependent representation of how energy is partitioned in the system, describing the intrinsic and extrinsic forces acting on the particle.

This is especially useful for systems with driven and stochastic forces, providing insights into the vibrational and dissipative characteristics of the system. For a harmonically bound particle in thermal equilibrium, the PSD characterizes the system by relating its thermal energy to the fluctuating forces that cause the particle's motion and is given by [10]:

$$S_{xx}(\omega) = \frac{2K_B T\,\gamma}{m[(\omega^2 - \omega_0^2)^2 + \gamma^2\omega^2]} \tag{1.1.5}$$

where K_B is the Boltzmann constant, T is the effective temperature, γ is the damping coefficient, m is the particle's mass, ω is the angular frequency, and ω_0 is the resonance frequency. The resonance frequency corresponds to the frequency where the particle oscillates naturally due to external restoring forces. The damping coefficient accounts for how frictional forces dissipate the system's energy, while the thermal energy drives random fluctuations in position.

This analysis is particularly useful in understanding Brownian-like motion in non-equilibrium systems, as the PSD is used to extract the effective temperature, damping coefficient and the resonance frequency from the experimental data.

1.1.1.4 Mean Square Displacement

The mean square displacement (MSD) characterizes particle motion by describing the time evolution of the particle's average displacement from its initial position, expressing its dynamic behavior and the forces acting on it. For non-equilibrium and equilibrium systems, this is useful in quantifying the mobility and transport properties of particles. For instance, in a one-dimensional diffusive system;

$$MSD(t) = \langle \big(x(t) - x(0)\big)^2 \rangle \tag{1.1.7}$$

where $x(t)$ is the particle's position at time (t). In a Brownian system, the MSD grows linearly with time, a characteristic of normal diffusion as:

$$\langle \Delta x^2(t) \rangle = 2Dt \tag{1.1.8}$$

where D is the diffusion coefficient. This linear relationship reflects the random motion of the particle as it collides with surrounding molecules, driving the particle's motion as in a system with thermal fluctuations.

In non-equilibrium systems, the MSD can deviate from this simple linear relationship, and exhibit a power law relationship:

$$MSD\ (t) \propto t^{\propto} \tag{1.1.9}$$

This power-law relationship more broadly describes motion observed in non-equilibrium dynamics, including systems subject to external forces, confinement, or interactions with complex media.

1.2 Experimental design

We consider a simple system consisting of a vibrating platform and a single sphere. This chapter details experiments exploring the sphere's dynamics, and in particular (a) the methodology with which the experiments were conducted, (b) how the data was analyzed, and (c) how the results were contextualized and compared to the fundamentals of equilibrium statistical physics.

1.2.1 Setup to drive macroscopic spheres into random motion with ultrasonic vibrations

An overview of the acoustic vibration setup is provided in Figure 1.1. The setup consists of two sections: the vibration scheme and the detection scheme.

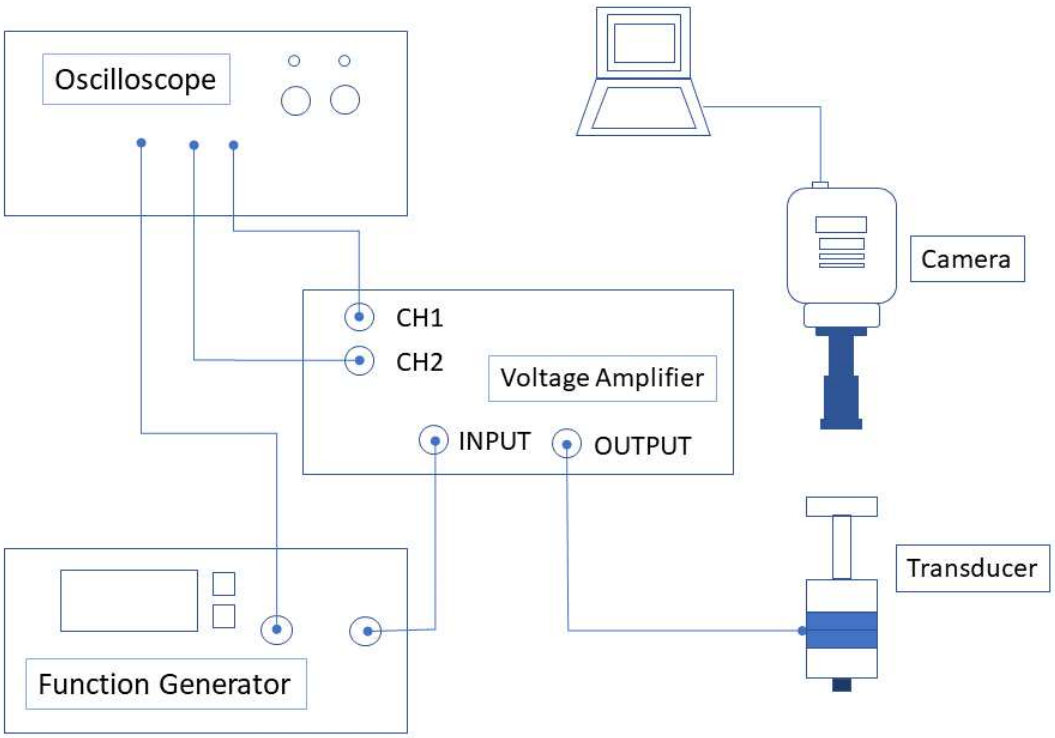

Figure 1.1. *Experimental set-up. The setup comprises two main parts. The vibration source comprises a function generator, whose signal is monitored by an oscilloscope, connected to a voltage amplifier to enhance the signal. The oscilloscope also monitors the amplified signal. The signal is sent to an ultrasonic transducer to provide the required vibrations. The detection side comprises a camera with sufficient magnification to observe any motion of the macroscopic particles. These signals are sent to a computer for visualization and analysis.*

1.2.1.1 Electromechanical vibration scheme

The core of the acoustic vibration source is a bolt-clamped Langevin transducer (STH-544-3030A, Sunnitec Piezoelectric Technologies, resonance frequency of 28kHz). The commercially available transducer is a typical resonant single-axis ultrasonic transducer, consisting of a sandwich structure containing a back mass, a stack of piezoelectric ceramics, and a front mass as shown in Figure 1.2a.

The front mass is designed to be a mechanical amplifier and constructed to have a smaller diameter (20 mm) than the rest of the structure (30 mm), creating a step as shown in Figure 1.2b. The commercially available transducer is modified by replacing the original (cylindrical) front mass with an aluminium mass of diameter 10 mm, and a concave 'horn' diameter 20 mm and radius of curvature 58 mm at the base. This smaller diameter and concave base serve to amplify the acoustic vibrations on the surface. The altered transducer is shown in Figure 1.2b.

The instrumentation to provide and amplify the acoustic vibrations as well as monitor the input and output current and voltage are shown in Figure 1.1. The transducer's vibrations are induced by a 40Hz dual function pulse generator (TGF4042, Aim TTi), and this signal is

amplified to ensure sufficient power in the system (PX200 Voltage Amplifier, PiezoDrive). A 60MHz four-channel digital storage oscilloscope (TBS1064, Tektronix) monitors both the voltage and current supplied to the system, as well as the response of the transducer to the provided signal.

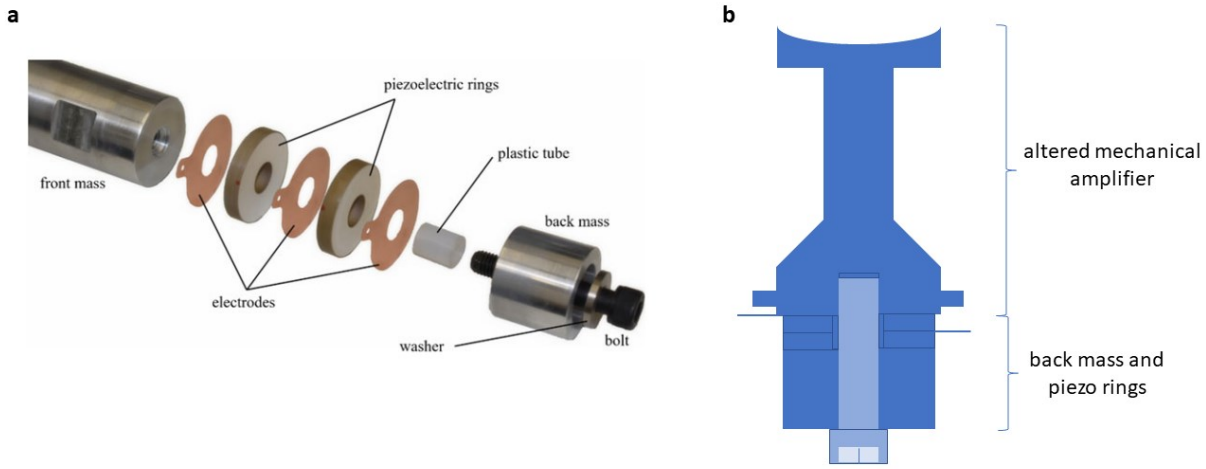

***Figure 1.2**. Electromechanical vibrator. The system uses a modified commercially available resonant single-axis ultrasonic transducer. **(a)** The transducer features an aluminium back and front mass sandwiching a pair of piezoelectric ceramics. This image has been drawn from Andrade et al* [11]*; published under a Creative Commons license (CC-BY 4.0) **(b)** The front mass also contains a mechanical amplifier which has been modified to increase the displacement amplitude generated by the sandwich structure as well as focus the acoustic vibrations on the surface of the transducer.*

1.2.1.2 Confining surface and the spring constant

The spring constant, k, characterizes the restoring force acting on the particle as it deviates from its equilibrium position. We approach the calculation of the spring constant by analyzing the surface curvature, which effectively dictates the shape of the potential well confining the particle. When a particle is confined to a curved surface under the influence of gravity, the local curvature of the system creates a restoring force that can be approximated by a harmonic potential near the equilibrium position.

The gravitational force, coupled with the curvature of the surface, leads to a potential well that can be modeled as quadratic near the minimum. To see this, we first consider the equation [12]:

$$U(x) = mgh(x) = \frac{1}{2}kx^2 \tag{1.2.1}$$

where the height, $h(x)$ is directly related to the curvature of the surface and $mgh(x)$ represents the gravitational potential energy of the particle. As shown in Figure 1.3:

$$h(x) = r\sqrt{1 - \left(\frac{x}{r}\right)^2} \tag{1.2.2}$$

Considering Equation 1.2.1 and the derivation presented in Appendix A, we can deduce from this the spring constant, k:

$$k = \frac{mg}{r} \tag{1.2.3}$$

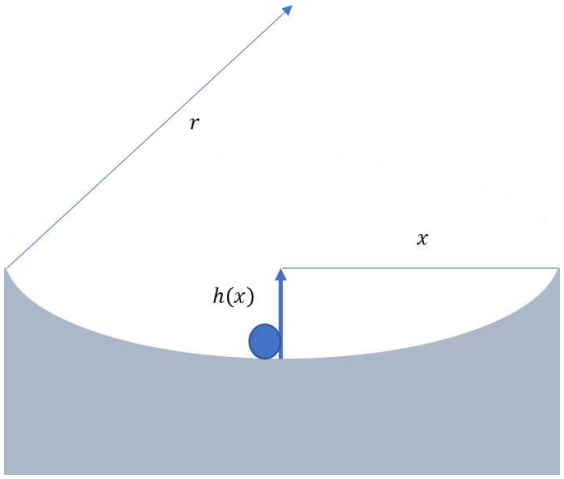

Figure 1.3. *Schematic of the particle on the curved surface, showing the geometric dimensions of the surface curvature.*

We calculate a numerical value of $k = (2.2 \times 10^{-3})\ \mathrm{kgms}^{-1}$. This approach, grounded in the geometric properties of the surface, provides an independent way to determine the confinement strength of the system.

Additionally, considering the relationship between the spring constant of the system and the resonance frequency of the particle motion [13] as:

$$\omega_0 = \sqrt{\frac{k}{m}} \tag{1.2.4}$$

Expressed in Hertz, as the cyclic frequency,

$$f_{resonance} = 1.3\ \mathrm{Hz}$$

1.2.1.3 Particles

We use commercially available well-characterized soda lime glass microspheres (SLGMS-AG-2.5, Cospheric, density 2.5g/cc, diameter 1000 μm). These solid microspheres are silver coated, making them conductive.

1.2.2 Detection scheme

The image capturing system consists of a GoPro camera mounted on a stable support (Hero Black). Images are taken at 240 frames per second, using a HDR widescreen capture. The camera's resolution is set at 1920 X 1080 pixels. Each video runs for at least two minutes to allow for long observation times of the particle's trajectory and dynamics. A typical sample image is shown in Figure 1.4b. With the imaging settings described, the typical diameter of the imaged particle is $d \sim 86$ pixels on average.

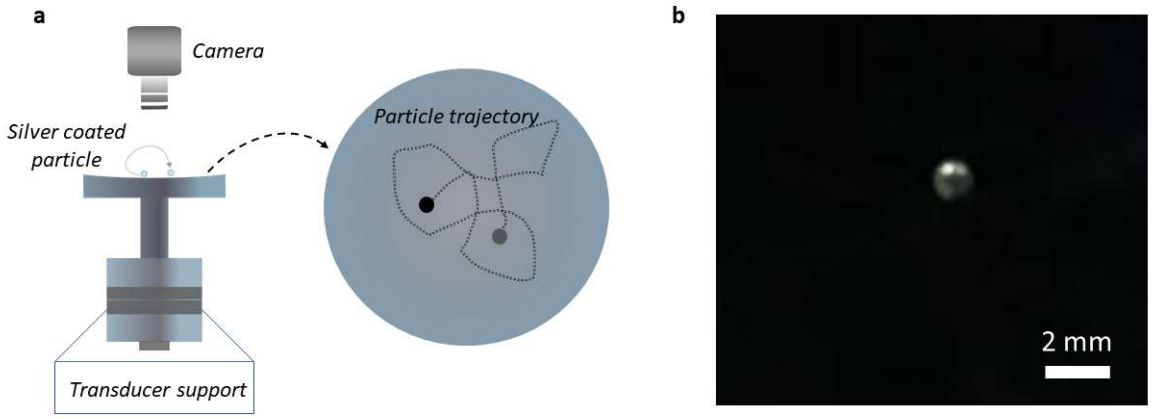

Figure 1.4. *Image capturing system.* ***(a)*** *The transducer is supported to limit movement during vibrations. The particle is observed from the top, with the most of the surface of the transducer visible in frame to ensure all the particle's motion is recorded.* ***(b)*** *A sample frame from the recorded videos.*

1.2.3 Particle tracking

To quantitatively characterize a particle's motion, we apply a particle tracking program in MATLAB. We calculate the center of mass, surface area, and diameter of the single identified particle by applying a Gaussian thresholding in each frame, and binarizing to extract the weighted centroid and area of the detected particle. MATLAB's *regionprops* function identifies areas of bright regions, by finding unique objects in binary images using 8-connected neighborhoods for 2-D images, and maximal connectivity for higher dimension images (MathWorks, 2023). Next, an area-based filter is applied to further filter the particles and ensure only one particle of interest is identified in each frame. A pixel to meter scaling is calculated using the size of the particle as provided by the manufacturer and the pixel diameter determined by the MATLAB code.

Particles are linked from one frame to the next by searching the vicinity of their previous center of mass for a particle of similar shape and size within the limits of its diameter. Once the (*x, y*) position of the particle is identified and stored, the velocity of the particles is calculated based on their displacement between successive frames. The frame rate of the videos determines the time difference, and the displacement in x and y is calculated by simply subtracting the previous frame's position from the current one. The velocity is then

obtained by dividing the displacements by the time difference as given by the camera's frame rate.

1.2.4 Trajectory analysis

Quantifying the mean square displacement (MSD), Power Spectral Density (PSD) and Probability Distribution Function (PDF) of the particle positions and trajectory is useful in calculating physical parameters relevant to the system like effective temperature, T_{eff}, damping coefficient, γ, spring constant, k, and resonance frequency, ω_0. Additional analysis includes the displacement correlation for a qualitative characterization of the particle motion. To visualize and extract information about the particle's motion, the MATLAB tracking software plots the particle positions, frame by frame. Further analysis on the particle trajectory includes calculating the PDF for the particle's position and velocity, MSD and PSD as described in the following sections.

1.2.4.1 PDFs and heatmaps of particle position and velocity

The particle position is centered at the origin, and then fit to a Gaussian distribution using MATLAB's *fitdist* function, which fits probability distribution object to data — in this case a normal distribution — and provides the mean and variance parameters (MathWorks, 2023). A range of values is then defined based on the minimum and maximum of the centered data and used to calculate the PDF across the possible values of (*x, y*) positions. A histogram is also plotted applying binned position data. A similar treatment is applied to the velocity data in *x* and *y*.

To calculate the 2D histogram (or probability density) of the position and velocity components, we use MATLAB's *histcounts2* function. This function bins the joint (*x, y*), position and velocity data into a 2D grid of equally sized bins with each bin corresponding to a specific region where the particle is tracked, normalizing the count in each bin to form a probability density function. Unlike independent histograms for *x* and *y*, which would ignore correlations, this approach allows us to account for any interdependencies between the two dimensions. By defining symmetrical edges around zero in both *x* and *y*, the bins capture the spatial distribution relative to a central equilibrium position. We then visualize the resulting 2D histogram as a heatmap using MATLAB's *heatmap* function, providing a comprehensive view of the particle's spatial and velocity distributions, and highlighting any correlated behavior in *x* and *y* directions. This joint PDF offers a more complete understanding of the particle's movement dynamics and spatial confinement, revealing areas of high probability density that indicate where the particle is most frequently found.

1.2.4.2 **PSD calculation**

We calculate the PSD by taking the squared magnitude of the Fast Fourier Transform (FFT) of the (*x, y*) positions and normalizing it by the product of *N,* the number of positions, and *Fs,* the sampling frequency to ensure proper scaling of the PSD. We apply the FFT using MATLAB's *fft* function, which computes the discrete Fourier transform of the signal and decomposes the time-domain signal into its constituent frequencies. Since the FFT output is symmetric, only the first half of the spectrum is retained. By focusing on the first half of the spectrum and correcting the amplitude, the code ensures that the PSD values are accurately represented.

1.2.4.3 **MSD calculation**

To calculate the MSD, a loop iterates over possible time lags (τ), calculating the displacement between the particle's position at time (i) and $(i\ +\ \tau)$ in (x, y).

Specifically, for each time lag:

$$\langle \Delta x^2(\tau) \rangle = \frac{1}{N-\tau} \sum_{i=1}^{N-\tau} \big(x(i+\tau) - x(i)\big)^2 \tag{1.2.7}$$

$$\langle \Delta y^2(\tau) \rangle = \frac{1}{N-\tau} \sum_{i=1}^{N-\tau} \big(y(i+\tau) - y(i)\big)^2, \tag{1.2.8}$$

where τ is the time lag, N is the number of frames, $x(i)$ and $y(i)$ the particle positions at time i and $x(i+\tau)$ and $y(i+\tau)$ are the particle positions at time $(i+\tau)$. Finally, the MSD values are plotted on a log-log scale, with different colors representing the MSD in the x direction, y direction and the averaged MSD.

1.3 Results and analysis of trajectories

This section presents the results of the experimental study of the particle dynamics. We present visualizations of particle behavior by showcasing particle trajectories in Section 1.3.1, visualize position and velocity probability densities and discuss the implications of these distributions in 1.3.2 and 1.3.3. Section 1.3.4 presents the power spectral density and applies the theoretical frameworks discussed in the introduction to offer insights into some physical properties of the system such as effective temperature and damping coefficient. In Section 1.3.5, we present the displacement correlation to characterize the dynamics of the particle under vibration. In Section 1.3.6, we discuss mean square displacement and further qualitatively characterize the particle's dynamics. Finally, in Section 1.3.7, we present a

representation of the systematic effective temperature, graphically visualizing the effect of different voltages, and consequently, different levels of energy fed into the system by way of vibrations.

1.3.1 **Particle trajectory**

A typical particle trajectory at a moderate vibration amplitude (200 mVpp) is shown in Figure 1.5a. It is clear that the particle explores several millimeters around the surface whenever the voltage of the transducer is sufficiently high, with the observed area explored increasing with the vibration amplitude. Within this range, the particle's exploration is largely symmetric in the *x* and *y* directions, indicating the system is isotropic. When the particle reaches the edges of the explored area, it performs parabolic arches indicative of the influence of gravity pulling the particle back into the trap as the curvature of the platform becomes larger nearer to the edge. At higher voltages, greater than 600 mVpp, the particle also exhibits noteworthy vertical jumps on the surface. In that regime, we observe greater distances between frames, manifesting as a more discontinuous motion across the same distances in Figure 1.5b in comparison to the more connected one shown in Figure 1.5a.

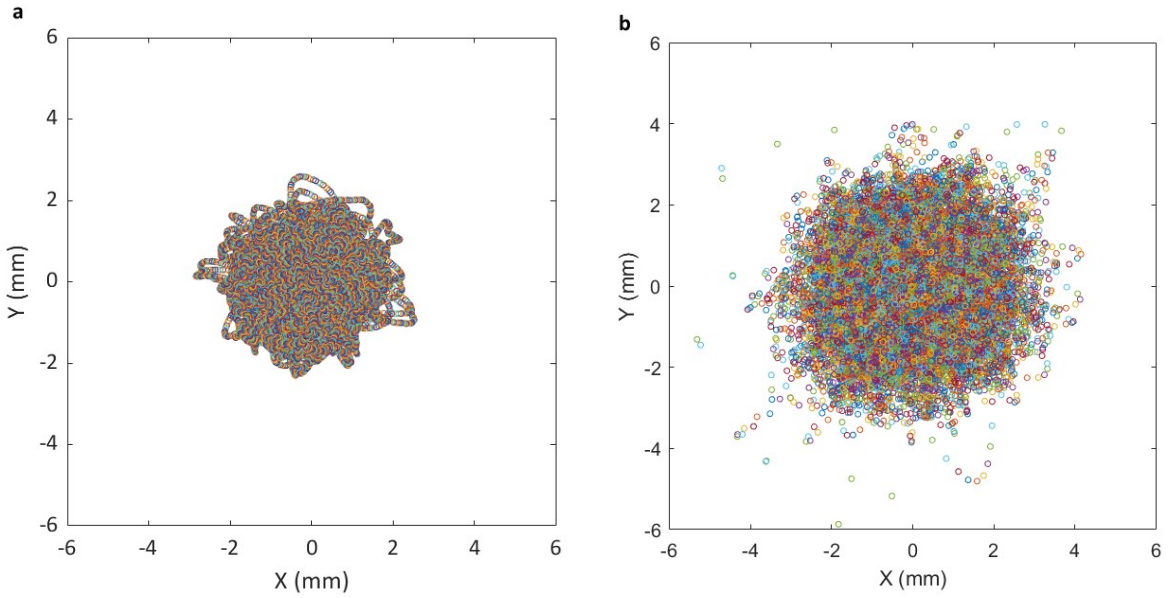

Figure 1.5. *Particle trajectories. Trajectories of the same particle driven at different voltages.* ***(a)*** *Particle trajectories driven at 200mVpp. The motion is isotropic and connected, indicating a continuous horizontal motion on the surface of the transducer. The range of movement is also tight, only 3mm from the equilibrium position* ***(b)*** *Particle trajectories driven at 600mVpp. The motion is more widespread, about 5mm from the average position. The motion is also discontinuous, due to observed vertical jumps experienced by the particle. Different voltages mean different vibration energy fed into the system, indicating a potential effective temperature as a function of voltage. Note the difference in particle motion, with the system driven at higher voltage not horizontally bound.*

1.3.2 **Position distribution**

To begin exploring connections between the observed particle motion and classical results of statistical mechanics, we plot the positional probability distribution of the particle as sampled over time. The PDF of the particle positions captures more rigorously how the particle explores the space around its equilibrium position. By fitting the position data to a Gaussian distribution as described in Section 1.1.1, we can extract an estimate for the effective temperature.

Figure 1.6 shows the spatial PDF for a particle vibrated at 200 mVpp. In panel (a), we show the 2D version of this as a color map, with red corresponding to high-probability regions and blue corresponding to low-probability regions. The heatmap is useful to visualize the spatial distributions of the particle, highlighting the positions most favored by the particle and effectively showcasing the potential confinement areas and barriers in the particle's motion on the surface. As with the trajectory in Figure 1.5, we see that the particle spends most of its time near the center of the trap. We also observe that the distributions are isotropic; the particle does not have a preferred axis of motion.

In panel (b), we present collapsed versions of this data for the x and y motion, respectively. If the position distribution is perfectly Gaussian, i.e., if the particle tends to remain near the center of the potential well with a much lower probability of being found near the edges, the particle can be considered to be bound to a harmonic potential.

Now, considering a Brownian-like motion, the probability of finding the particle in a particular position can be expressed as a Gaussian distribution [9] as derived in Appendix B:

$$P(x) = \frac{1}{\sqrt{2\pi\sigma^2}} e^{\frac{x^2}{2\sigma^2}}, \tag{1.3.1}$$

where

$$\sigma^2 = \frac{K_b T}{k}\ . \tag{1.3.2}$$

Considering we have the spring constant, k, previously calculated as a function of the curvature of the system, we can extract the effective temperature of the system from the variance of the distribution. The calculated value is near equivalent in both X and Y, supporting the idea of an isotropic motion of the particle on the surface. In X, the calculated effective temperature is 3.0×10^{11} K, while Y has an effective temperature of 2.8×10^{11} K, averaging to 2.9×10^{11} K.

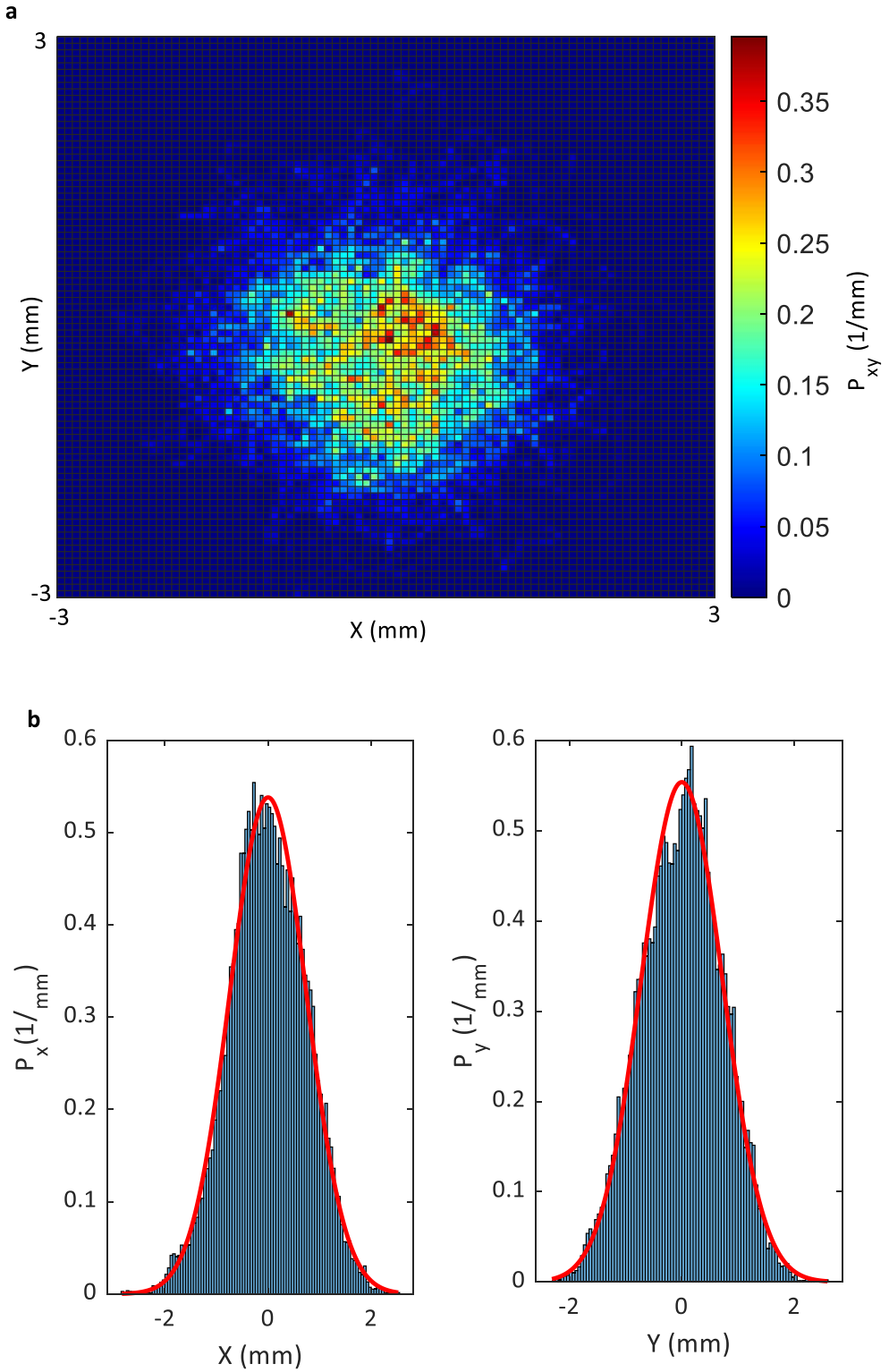

Figure 1.6. *Positional distribution of particle. (**a**) Heatmap of the particle's position showing the diffusion patterns and confinement regions in the motion of the particle. The particle has a higher frequency of appearance in the normalized central position, with a much lower probability of being found on the edges of the surface. **(a)** Normalized histogram of the position of the particle on the surface over time to visualize the spatial distribution of the particle fitted to a Gaussian and a Probability Distribution Function (PDF). Note that the PDF and Gaussian distribution fits are equal. These distributions form the basis for the calculation of variance of the particle's position and the spring constant of the system.*

1.3.3 **Velocity distribution**

Figure 1.7 shows the velocity distribution of a particle driven at a 200mVpp. In panel (a) we show a color map that visualizes the directional preferences in the particle's motion. It also presents the most common velocity of the particle, with red corresponding to high probability regions and blue lower probability regions. Note the symmetric and centered distribution, affirming the isotropy of the particle's motion; there are no directional preferences. Panel (b) shows the normalized histogram of the velocities of the particle on the surface over time. This is useful in visualizing the dynamics of the particle, and is fitted to a PDF. This panel illustrates a smooth, narrow peak centered at zero. Notice the Gaussian and PDF are equivalent. The peak's sharpness indicates the concentration of velocity values around the equilibrium, while the symmetry of the distribution further indicates an absence of directional bias in the particle's motion. If the PDF is consistent with the Gaussian form of the Maxwell-Boltzmann distribution, the fits provide a basis for calculation of the effective temperature of the system by connecting the probability of the velocity to the kinetic energy of the particle.

The Maxwell-Boltzmann distribution describes the velocity of particles in thermal equilibrium, providing the probability of a given velocity as:

$$P(V_x) = \frac{m}{\sqrt{2\pi k_B T}} e^{\frac{-mV_x^2}{2K_B T}}, \tag{1.3.3}$$

where $\frac{m}{\sqrt{2\pi K_b T}}$ is the normalizing factor. This expression is derived from the Boltzmann distribution and the Langevin equation as shown in Appendix C.

When we fit the observed velocity data to the Maxwell-Boltzmann model, there is a strong agreement between the model and the observed data as shown by the PDF and the histogram of the experimental data in the narrow, centered peak in both the PDF and the heatmap. This agreement confirms that the particle's motion is consistent with the predictions of statistical mechanics at thermal equilibrium. This validation also allows us to extract the effective temperature of the system, which in this case is 2.9×10^{11} K for velocity in x and 2.6×10^{11} K in y. This number compares well with the temperature extracted based on the position distribution, tacitly confirming the "equipartition" of energy between different degrees of freedom.

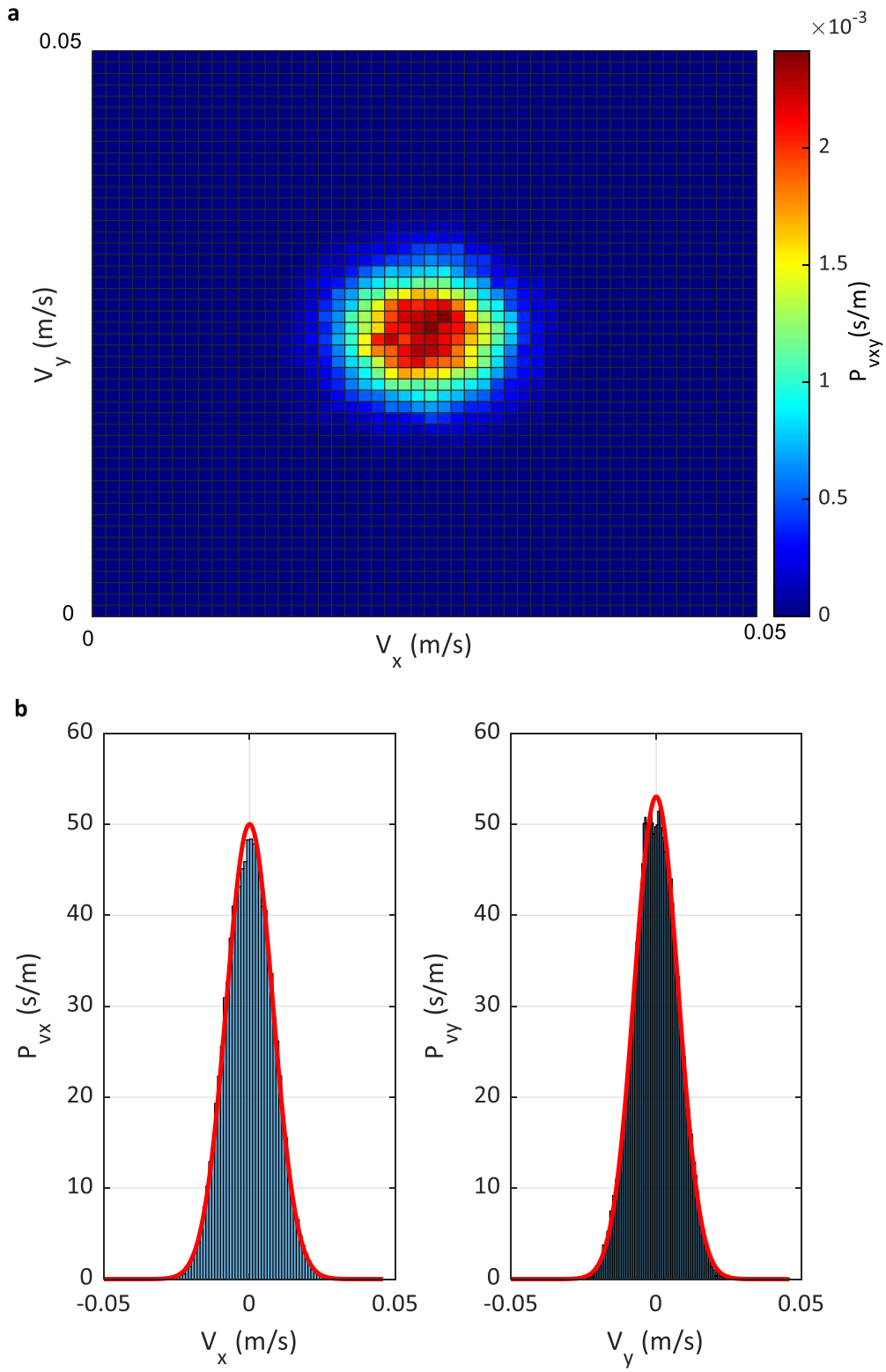

Figure 1.7. *Velocity distribution of particle.* ***(a)*** *Heatmap distribution of the particle's velocity, visualizing the most common velocity of the particle. This visualization displays the directional preferences in the particle's motion. Note the distribution is narrow and centered, reflecting the thin velocity distribution peak in* ***(b)****. The heatmap also indicates a mostly uniform average kinetic energy of the particle.* ***(b)*** *Normalized histogram of the velocities of the particle on the surface over time to visualize dynamics of the particle, fitted to a Gaussian and a Probability Distribution Function (PDF). Notice the Gaussian and PDF are equivalent. The fits provide a basis for calculation of the effective temperature of the system by connecting the probability of the velocity to the kinetic energy of the particle as per the Maxwell-Boltzmann distribution.*

1.3.4 **Power Spectral Density**

To further characterize the positional fluctuations of the particle, we use a Power Spectral Density (PSD) analysis. The PSD, as derived in Appendix D, corresponds to an underdamped driven oscillator, quantifying effective temperature, resonance frequency and damping coefficient. The shape of the curve also provides a description of the system's spectral behavior, revealing how the energy of the particle's motion is distributed across different frequencies.

Figure 1.8 shows the PSD of the particle's position in x (Figure 1.8a) and y (Figure 1.8b) over a range of frequencies. Using a log-log plot, we present the experimentally obtained data (blue) and the fitted theoretical model (red). The fitted frequency range is limited to 0.1 - 20 Hz, excluding the low frequency (room) noise and the high frequency (measurement) noise. The plot features a distinct peak at one frequency, the resonance frequency ($f_{resonance} = 1.7$ Hz). The location of this peak corresponds well with the earlier estimation based on the curvature of the vibrating surface ($f_{resonance} = 1.3$ Hz, Equation 1.2.6). The width of this peak reflects the level of damping in the system, with a sharper peak indicating lower damping and oscillations that are more persistent.

Assuming an underdamped driven system, the PSD of the particle's position fluctuations can be described by Equation 1.1.5 as:

$$S_{xx}(\omega) = \frac{2K_B T\,\gamma}{m[(\omega^2 - \omega_0^2)^2 + \gamma^2\omega^2]} \tag{1.1.5}$$

where K_B is the Boltzmann constant, T is the effective temperature, γ is the damping coefficient, m is the particle's mass, ω is the angular frequency, and ω_0 is the resonance frequency.

The model fits the observed data well, as seen in the alignment of the theoretical curve with the experimental fit in the range excluding the low and high frequency noise in Figure 1.8. We extract an effective temperature, $T_x = 2.3 \times 10^{11}$ K, $T_y = 1.9 \times 10^{11}$ K. These values closely correspond to the effective temperatures extracted from the velocity and positional distributions ($T_x = 2.9 \times 10^{11}$ K, $T_y = 2.6 \times 10^{11}$ K for velocity and $T_x = 3.0 \times 10^{11}$ K, $T_y = 2.8 \times 10^{11}$ from the positions). From the fit we also determine the damping coefficient, $\gamma = 3.2\ \mathrm{s}^{-1}$. The damping coefficient quantifies the viscous damping experienced by the particle. Since the damping coefficient, γ, is less than the resonance frequency, ω_0, we are able to characterize the system as underdamped [14]. A lower damping coefficient suggests lower resistance that allows the system to oscillate; the damping only slows down the oscillations, rather than completely suppressing them.

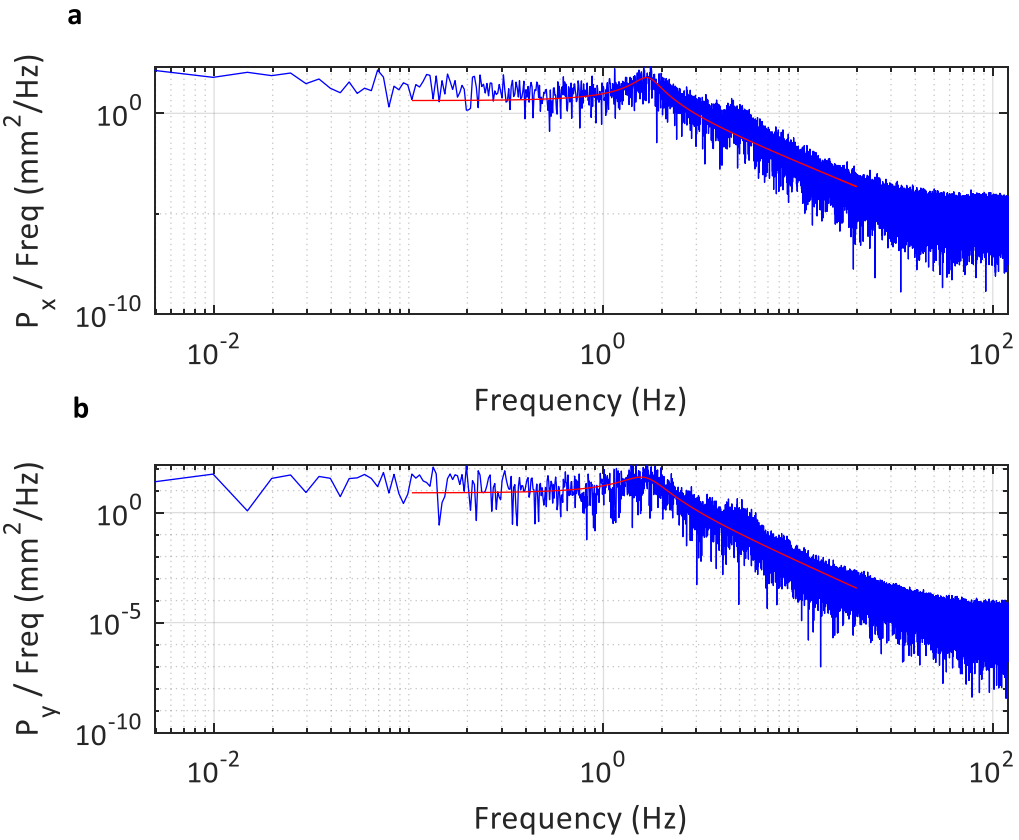

Figure 1.8. *Power spectral Density (PSD) of positions in X and Y. A log-log plot of the PSD analysis of the particle's motion in the* ***(a)*** *x-direction and* ***(b)*** *y-direction is shown in mm^2 /Hz. The PSD plots are shown for the experimentally obtained data (blue) and the fitted theoretical model (red). The fitted frequency range is limited to 0.1 - 20 Hz, excluding low- frequency and high-frequency noise. These fits are used to extract the resonance frequency, ω_0, damping coefficient γ, and effective temperature, T_{eff} for comparison with the velocity and position calculated values.*

1.3.5 **Displacement correlations**

To qualitatively describe the temporal dynamics of the particle's displacement on the surface, we analyze the displacement correlation as a function of time lag. Figure 1.9 illustrates the correlation values across a range of time lags, with the x-axis indicating time lag in seconds (Δt) and the y-axis representing the correlation coefficient. The curve exhibits a prominent initial peak at a time lag of zero, reflecting the strong correlation of the particle's position with itself. The curve then evolves to exhibit smooth oscillatory behavior, indicating periodic motion. The presence of a smooth relatively long periodic oscillation suggests the system operates as an underdamped harmonic oscillator.

This analysis complements our earlier examination of the Power Spectral Density (PSD) of the particle's positional fluctuations, describing the damping characteristics of the system. The correlation of displacement reveals a similar underdamped system; the relationship between the damping observed in the PSD and the temporal decay of correlation underscores the interconnected nature of these analyses. Both approaches provide insight into the system's dynamics, illustrating how the damping influences the persistence of correlations over time

and the overall fluctuation behavior of the particle. The time lag has been limited to 4.5s, with continuous periodic oscillatory behavior that lasts a long time as shown comparatively in Appendix E.

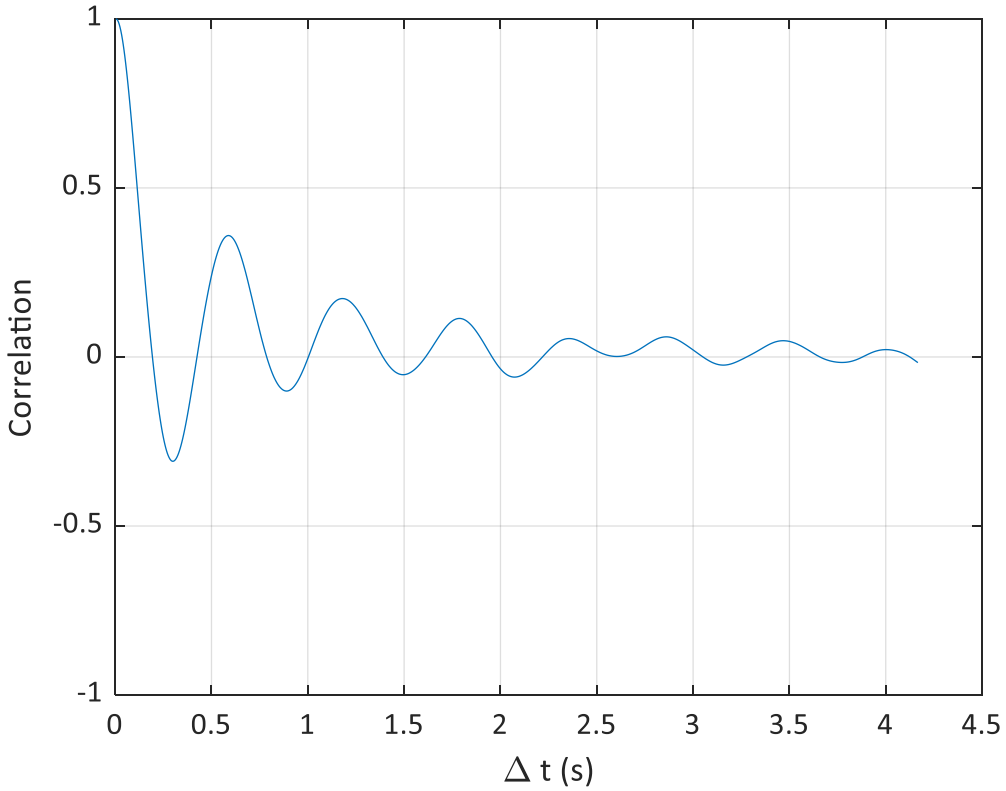

Figure 1.9. *Temporal correlation. The displacement correlation function, showing the correlation in particle positions over time. This visualizes the memory effect in the particle movements and characterizes persistence in the particle's motion. Note the oscillatory behavior of the curve, indicating the presence of periodic or oscillatory motion in the system.*

In an ideal Brownian motion scenario, we would expect the displacement correlation to decay monotonically without oscillations, indicating purely diffusive behavior. However, the observed oscillations suggest a more complex behavior where a restoring mechanism, i.e. curvature of the surface, influences the particle's movement.

1.3.6 **Mean square displacement**

To characterize the motion of the particle across different temporal regimes, we analyze the mean squared displacement (MSD). Depending on the form of the plot as a function of time, the particle motion can be inferred as either diffusive, ballistic, super diffusive or sub diffusive as referenced in Equation 1.1.9. In diffusive behavior, the MSD evolves linearly with time but deviations from this linear trend suggest more complex dynamics, where the particle's movement does not adhere to a single power law. Instead, the movement exhibits varying characteristics at different time scales.

In Figure 1.10, we show the MSD plotted against time on a log-log scale. Notice the MSD in the x direction (red) and the y direction (green) are aligned, revealing an agreement, or isotropy, in the motion of the particle in both dimensions as well as an equivalent average (blue). The plot highlights different regions of the particle's motion, where distinct patterns emerge: an initial linear region at short times with a slope ≈ 1.5 at $10^{-3} < t < 10^{-1}$ s, oscillatory behavior at intermediate times ($10^{-1} < t < 10^{1}$ s), and eventual plateau at longer timescales ($10^{1} < t < 10^{2}$ s), suggesting different dynamics across different regimes.

Considering the power law introduced in Equation 1.1.9:

$$MSD\ (t) \propto t^{\propto} \tag{1.1.9}$$

the value of the exponent characterizes the particle's diffusive behavior. A linear relationship on the log-log scale suggests that the particle's movement follows a power-law behavior; the slope of the curve provides the exponent, which determines whether the motion is ballistic ($\propto = 2$), super diffusive ($1 < \propto < 2$), diffusive ($\propto = 1$), or sub diffusive ($\propto < 1$) [15], [16], [17].

At short timescales ($10^{-2} < t < 10^{-1}$ s) the curve has a slope ≈ 1.5, revealing a super diffusive regime, where the particle's motion is largely vibration driven. At intermediate timescales, the particle transitions to oscillatory behavior indicating that external factors, such as the curvature of the surface, influence the particle. These oscillations define a harmonic oscillator response, where the particle is momentarily pushed by the surface's curvature before being pulled back, preventing it from fully diffusing away again to a non-monotonic MSD.

At longer timescales, the MSD plateaus, suggesting that the particle becomes confined. This confinement can be attributed to the particle being trapped on the surface, due to the equition of the driving forces of the vibration and the systematic spring response due to the shape of the surface. The observed behavior underscores the influence of the surface's geometry and the external driving forces in dictating the particle's motion, leading to a multi-regime dynamic that does not fit neatly into a simple diffusive model. The particle's motion is therefore not purely 'Brownian', but has more complex dynamics involved.

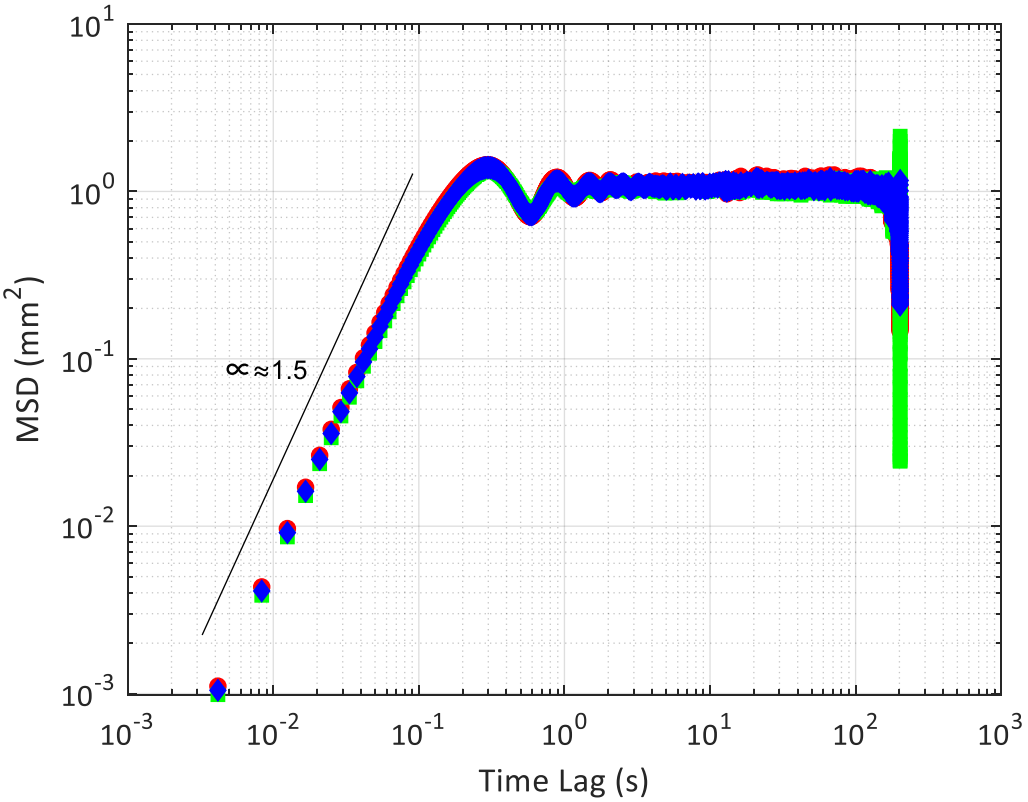

Figure 1.10. *Log-Log Mean Square Displacement (MSD) plot. The plot is presented on a log-log scale to showcase a temporal range of several orders of magnitude, highlighting different regimes of motion for long term and short-term behavior. Notice the MSD in the x direction (red) and the y direction (green) are aligned, highlighting an agreement in the motion of the particle in both dimensions as well as an equivalent average (blue). The MSD shows an initial linear region, with slope =1.5, oscillatory behavior, and eventual plateau, suggesting different dynamics across different regimes.*

1.3.7 **Effective temperature**

Temperature in the normal sense does not play a relevant role in the dynamics of the particle in the system under investigation. This is largely due to the size (1000 µm diameter) and mass of the particle (1.31×10^{-3} g) in comparison to the kinetic energy supplied by ambient temperature. We therefore define an effective temperature which is responsible for the motion of the relatively massive particle in this system. This temperature is therefore not a physical quantity, but rather an analogic descriptor governing the motion of the particle due to the driving energy from the ultrasonic vibrations.

An analysis of the distribution of particle positions also offers insights into the effective temperature as determined from the variance of the distribution and the systematic spring constant as per Equation 1.3.2. Additionally, considering the kinetic theory of gases and the equipartition theorem, the effective temperature has been extracted from the Maxwell-Boltzmann distribution of the velocities of the particle as in Equation 1.3.3. This value can also be extracted from the PSD analysis as shown in Equation 1.1.5.

Figure 1.11 showcases the effective temperature as a function of the square of voltage, particularly for voltages of 100 V, 200 V, 300 V and 600 V. The voltage squared plot provides a direct relationship to the energy input since energy is proportional to the square of the voltage ($E \propto V^2$) allowing for a more accurate representation of how temperature evolves with the energy input into the system. The temperature extracted using the velocity distribution is systematically higher than the PSD temperature. However, all measurements are in the same order of magnitude, with a similar evolution across amplitude, suggesting some agreement in the calculated effective temperature.

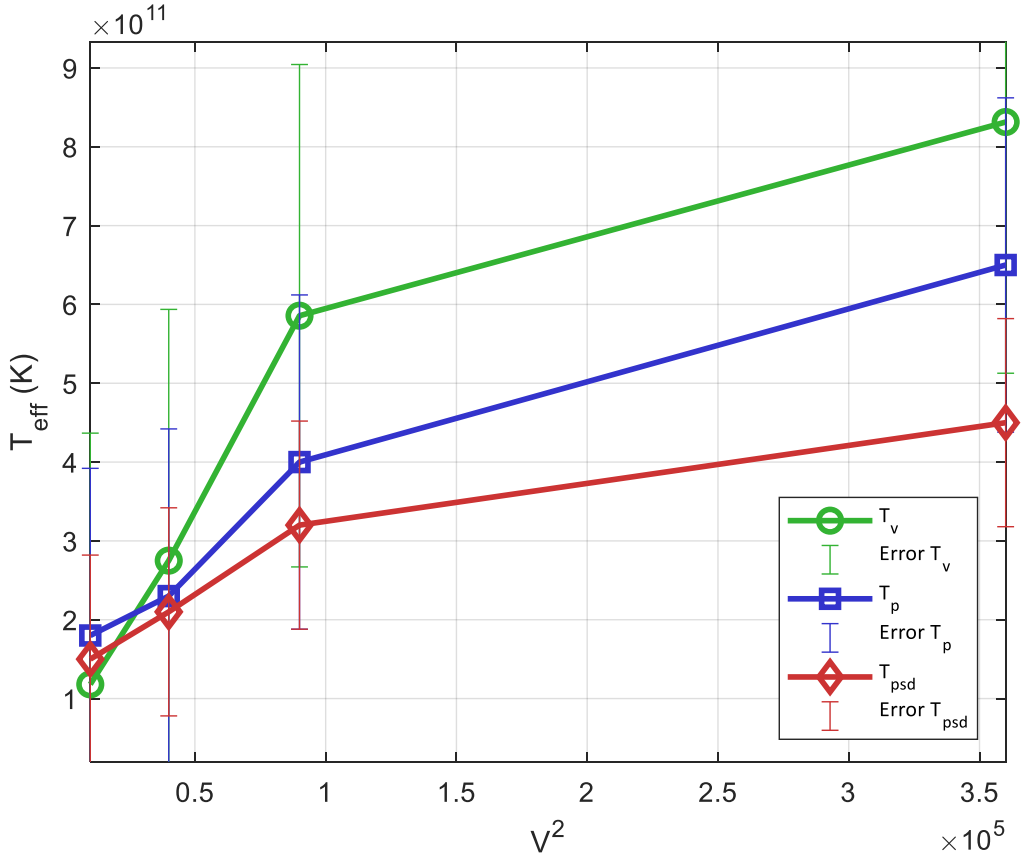

Figure 1.11. *Effective temperature as a function of voltage. The voltage values in this case informs the amplitude of the ultrasonic vibrations. Temperature calculated from the position distribution is shown in blue, from velocity distributions is shown in green, and the PSD temperature is expressed in red. The spread of values remains consistent for all recorded voltages. Notice that the calculated effective temperature evolves linearly as a function of voltage, suggesting the voltage is the indicator of energy fed into the system. By extension, this further shows that the calculated values can be considered 'temperature' in terms of energy driving the system.*

Noting that the temperature calculated using the PSD is consistently and considerably lower than that derived from the position and velocity distributions. This discrepancy can be attributed to the fact that the PSD measures position fluctuations, and the damping characteristics of the system play a bigger role in the measurement, which are smaller than the velocity fluctuations that contribute directly to the kinetic energy of the system and are heavily influenced by the ultrasonic vibrations introduced in the system. In an isotropic system where the distribution is Gaussian, velocity fluctuations generally exhibit greater variance, leading to a higher temperature when calculated from the velocity distribution. In

contrast, the PSD of positions is more sensitive to spatial correlations and the system's confinement, which can reduce the observed position variability, especially in the case of confined or underdamped systems. This results in a temperature measurement that reflects the reduced positional fluctuations rather than the full kinetic energy, explaining why the temperature derived from the PSD tends to be lower. This difference is consistent with the theory of particle dynamics, where velocity-based measurements are directly tied to the system's energy, while position-based measurements provide a more indirect and potentially underestimated view of the temperature [18] [19].

1.4 Conclusion

In this part of the thesis, we have set up experiments to explore whether a single particle system driven by ultrasonic vibrations obeys basic results of equilibrium statistical mechanics. Our experimental setup, highlighted in Section 1.2 allowed the generation of ultrasonic vibrations using a single axis Langevin transducer system, tuning for different amplitudes by using different voltages. The motion of the particles was monitored using a camera system for trajectory analysis. Statistical mechanics principles and ideas are considered to analyze the particle trajectories. We establish that the particle's dynamics are complex; the particle motion is not purely diffusive.

In the first part of our results, we study the distribution of the particle's position over time, as well as the velocity distributions. The analysis of the distributions of particle positions is modeled after a Gaussian distribution, connecting the systematic spring constant derived from the curvature of the system to the effective temperature of the system. The distribution of the velocities, also Gaussian, is modeled after a Maxwell-Boltzmann distribution and provides quantitative analysis on the effective temperature of the system. We find an increasing temperature value depending on the voltage driving the vibrations. Exploring the Power Spectral Density (PSD) of the particle's positions over time further quantitatively characterizes the system. As discussed, fitting the experimental data to the PSD for theoretical predictions effectively provides the damping coefficient, effective temperature and resonance frequency.

Additionally, we qualitatively characterize the particle's motion using temporal correlations, as well as the mean square displacement (MSD). These analyses offer perspectives into the motion of the driven particle. For this system, there are more complex dynamics at play, with $\alpha = 1$ at very short times, then $\alpha = 1.5$ at consequent short times, an oscillatory form at intermediate times and longer times reveals a plateauing in the MSD. This suggests dynamics that are not diffusive, and therefore not purely Brownian. The temporal correlation indicates an oscillatory pattern, and has characteristics of an underdamped system in a harmonic potential.

Finally, to quantitatively characterize the motion of the particle, we compared effective temperature of the different driven systems to showcase a relationship between effective energy fed into the system (voltage) and the observed quantity (effective temperature). Using the PSD, particle position distribution and velocity distribution, we quantify the effective

temperature, and observe an effective temperature in the same order of magnitude. We observe a linear relationship between the temperature and the energy, qualifying the system as a thermal response, like Brownian motion. However, the motion is not purely Brownian, as expected, since the curvature of the system also impacts the motion of the particle.

2 Microfabrication of particles with nano-scale 3D printing

2.1 Introduction

Microfabrication involves building structures at the micron or submicron scale. These designed miniaturized patterns, objects, or devices are useful in biophysics, pharmacology, medical biology, and nanotechnology [20]. In the 1950s, 1960s and 1970s, microfabrication was primarily applied in the design and fabrication of electronic components for the semiconductor industry, e.g., via photolithography. Later, other methods of microfabrication, such as ion and electron beam lithography, chemical and physical vapor deposition, self-assembly and 3D printing for a bottom-up approach were developed. There have been significant advancements in methods of microfabrication particularly with the necessity for smaller and more complex structures with expanded functionality.

Lithographic techniques of microfabrication are grounded in the occurrence of a chemical reaction on a 2D substrate [21], [22]. Broadly speaking, lithography uses either photons (photolithography) or electrons (electron beam lithography). For photolithography, light is used to transfer the desired geometric pattern from a photomask onto a photosensitive substrate. Electron beam lithography utilizes a highly energetic electron beam to apply the desired pattern, and provides a much higher resolution to create extremely fine patterns. While photolithography is fast, versatile and highly scalable, high-resolution photolithography remains very expensive and there are still a number of physical barriers to resolution, therefore truly 3D structures are not readily possible.

Etching involves the removal of material from a substrate either through wet etching or dry etching [23]. Wet etching involves the application of a liquid chemical (etchant) to the surface, selectively removing some materials to create a desired pattern. This process is continuous until the chemical process terminates and the desired structures emerge on the substrate. Dry etching uses plasma or gases to remove material through physical sputtering or chemical vapor. In physical sputtering, accelerated ions in vacuum physically knock atoms off the surface. Chemical etching involves reactions that form volatile chemicals that desorb off the surface. Depending on the exact etching method, etching offers high precision, versatility, and a high degree of complexity in the desired structure. It is also a good option for structures requiring a high aspect ratio. However, etching can require complex and expensive instruments as well as precise control of system parameters, which can otherwise lead to destruction of the surface.

In this thesis, I have learned and developed techniques in 3D nano printing. 3D nano printing works by depositing material layer by layer until a desired structure is achieved. This method has evolved through the years to allow very high resolution, enabling complex shapes and the endowment of additional novel properties. Laser nano printing in particular achieves an exceptional balance between resolution (down to ~1 micron), scale (up to ~1 mm), and speed. To create nanometrically resolved features and structures, this technique uses focused laser pulses to photopolymerize a photosensitive material. Advances in this technique have focused on improved photosensitive material, improved resolution, as well as increasing the

functionality of the microfabrication technique. I now describe below how I leverage 2PP for 3D nano printing, as well as explain my choice of design structures.

2.2 Two-photon polymerization

We perform nano-printing with an UpNano's NanoOne 1000 3D printing system, whose operating principle is based on two-photon polymerization (2PP). 2PP for fabrication can be applied both on the microscale (1 μm) and the macroscale (1000 μm), highlighting its advantages over other fabrication methods.

2.2.1 **Two-photon polymerization mechanism**

Photopolymerization nano printing relies on the polymerization of a resin by a focused laser beam of adequate wavelength. In principle, the technique can print down to the diffraction limit of optics. In practice, this resolution remains difficult to attain as the energy of the laser beam spreads over larger areas. In effect, single-photon polymerization is limited to feature sizes of half the wavelength of the incident light while 2-photon-polymerization (2PP) can achieve sizes that are significantly smaller [24]. 2PP works by Two Photon Absorption (TPA), the simultaneous absorption of 2 photons resulting in polymerization of photoresist [25]. TPA was first theorized by Maria Goeppert Mayer in her 1931 doctoral work and later experimentally observed in 1961 by Kaiser and Garrett during the excitation of CaF2:Eu. However, it is only in 1997 that Shoji Maruo and others directed the specific use of TPA for 3D nanofabrication. Typically, TPA functions by the principle that materials can transition to excited states through the simultaneous absorption of two photons, where the energy of a single photon is less than the energy gap between excited states. The initial absorption of the first photon promotes an electron to its excited state with extremely short lifetimes in the range of femtoseconds [26]. This mechanism ensures various advantages for resolution and precision. Femtosecond lasers bring a high concentration of photons in space and time by virtue of controlled "voxel" size, which is the minimum volume of a 3D pixel [26]. The voxel determines the resolution of the printed structures through the focusing of the laser. Figure 2.1b shows an ideal scenario; the center of the beam is focused onto a small area to optimize the size of a voxel by dosing the photoresist only fractionally above the polymerization threshold using high numerical aperture optics. This ensures that only the intended region is targeted.

When the laser is focused on a region, light induces a chemical reaction in the photoresist, mediated by a molecule known as a photo initiator. A photo initiator is a component of the photoresist that absorbs the irradiation, dissociating and generating free radicals, which initiate a chain reaction that propagates polymerization in the photoresist. The combined energy of the two photons matches the energy required to excite the photo initiators in the molecule to its reactive state. Concurrently, crosslinking occurs as polymer chains react with neighboring chains or functional groups, forming a three-dimensional network structure.

2PP therefore requires three main ingredients: a photosensitive resin, high-speed femtosecond lasers in the visible to infrared range, and a positioning stage to control the focusing of the laser. After scanning the laser focus in three dimensions to write the desired architecture, the remaining liquid is washed out using a solvent in the development phase.

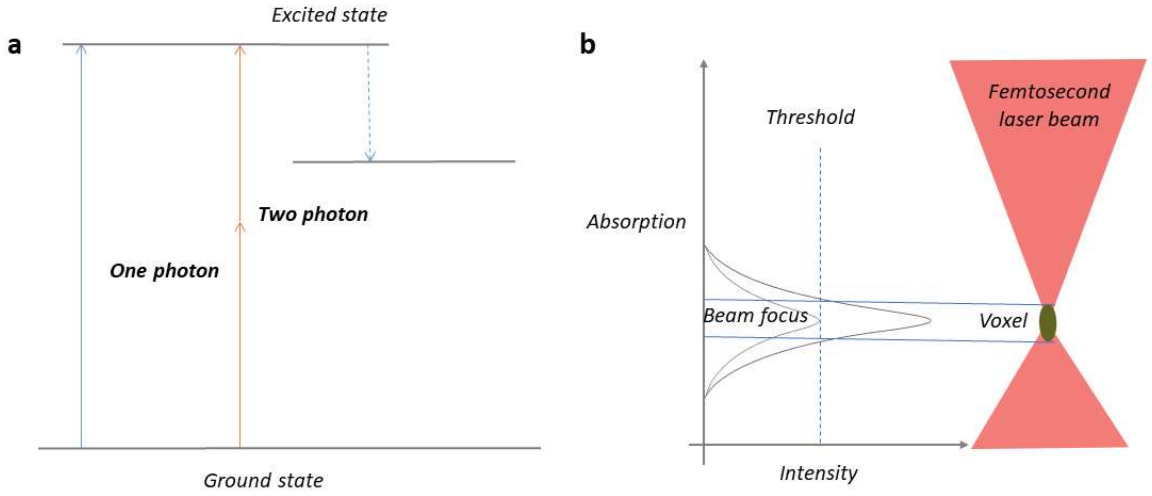

Figure 2.1. *2PP involves TPA, the simultaneous absorption of two photons leading to the excitation of an electron and the generation of radicals in the photo initiator for the photopolymerization to occur.* ***(a)*** *Simultaneous absorption, excitation of photons (orange) and virtual short-lived intermediate state (dotted blue) of the electron as well as the comparable one photon absorption (blue).* ***(b)*** *Photopolymerization by TPA is limited to the voxel, leading to a minimal surface interaction of the material with the light, other than the required focal volume.*

2.2.2 Materials and techniques of 2PP

The quality of 2PP for higher resolution structures depends on the optimization of laser input, choice of photoresist, and post-exposure treatment. In particular, choice of photoresist is significant for the desired properties in printed structures. Hanirayana and Shin [27] detail a few characteristics that are non-trivial for photosensitive resin. These include transparency in the visible and near IR frequency regime for deep laser penetration with no single photon excitation, fast curing speed and polymerization limited to the focal volume with minimal scattering.

In this thesis, I use a commercial suite of high performance 2-photon resins optimized to fully exploit the capabilities of UpNano's printing systems: UpPhoto, UpBrix and UpSol (UpNano gmbH). UpPhoto is a high-performance resin for functional components fully cured directly after 3D printing. UpBrix is a refractive index-matched resin, best for printing that requires a high NA objective and high cross-linking. It is therefore appropriate for ultra-high-resolution applications. UpSol is a sol-gel hybrid resin applied to the substrate by spin-coating. The resin is gel-like during printing, allowing the production of complex structures with overhangs and undercuts. This resin is also useful for printing free-floating elements, as we will further discuss below.

Below is a table detailing some of the properties of these two choices in resin:

Table 2-1. Comparison of photoresists

	Common objectives	*Fabrication speed*	*High aspect ratio*	*Sub-micron resolution*	*2.5D structures*
UpPhoto	20X, 10X, 5X	Medium	yes	N/A	N/A
UpBrix	40X	Medium	yes	yes	yes
UpSol	40X	Slow	yes	yes	yes

2.3 Electroless plating

In addition to microfabrication, I also explore creating conductive surfaces on the microfabricated structures. These efforts were intended to further process particles to explore non-equilibrium dynamics of particles under an electric field on a vibrating surface. We apply electroless plating, or autocatalytic metal plating, a non-electrolytic method of deposition from solution.

Discovered in 1946 by Brenner and Riddell [28] and later commercialized by Cahill and Zeblinsky [29], the process requires three main components: a metal salt, a catalytic surface and a reducing agent. The reducing agent supplies an electron to reduce the metal salt, forming a thin layer of metal on the catalytically active surface. The modern iteration of electroless plating, specifically electroless copper plating, was based on alkaline copper tartrate baths with formaldehyde as a reducing agent [29]. Optimal metal deposition is influenced by plating rates, choice of reducing agent, PH as well as complexing agents.

We apply a reducing agent on a copper salt for electroless copper plating. As a method of metal coating, electroless copper is much slower than electrolytically depositing copper, but has salient advantages for my thesis. First, the process ensures a thin uniform layer and features a high capability to deposit in deep creases, bores and blind holes, allowing us to metallize the complicated structures presented in this thesis. Second, electroless plating allows deposition on non-conductive (polymeric) surfaces, which cannot be achieved with electrolytic deposition.

2.3.1 **Mechanism**

Electroless plating involves a series of chemical reactions that occur on the surface of the substrate. These steps are activation, reduction, an autocatalytic process and a termination step. Activation involves creating a catalytic surface, since the chemical reaction responsible for metal deposition is not spontaneous. Additionally, a complexing agent is necessary to optimize the chemical reactions necessary for metal deposition. The reduction process is the main reaction, with a reducing agent supplying an electron to reduce a metal ion to a metal during deposition. The autocatalytic step has the deposited metal acting as a catalyst itself for further reduction reactions, allowing continuous deposition. Once the metal ions are depleted, the reaction terminates leaving a uniform layer of deposited layer. The thickness of

the deposited layer is therefore dependent on the concentration of the plating bath, allowing some control. Surface activation is accomplished by the application of a sensitizing agent, which creates adsorption sites on the particle surface, followed by the addition of a catalytic agent such as palladium chloride. This creates nucleation sites for the metal deposition, making this a crucial step for effective metal deposition. Deckert [29] details the importance of activation. Once the surface is activated, the substrate is immersed in an electroless plating bath containing metal ions, in this case a cuprite salt and a reducing agent, formaldehyde. Commercially, formaldehyde has been used extensively due to a combination of low cost, high effectiveness and ease of control of the system [30].

For copper (II), the following reduction reaction occurs on the surface;

$$\mathrm{Cu^{2+}} + 2\mathrm{e^-} \leftrightarrow \mathrm{Cu^\circ} \qquad (\mathrm{E^\circ} = +0.340)$$

For formaldehyde, E° depends on the pH of the solution:

$$\mathrm{HCOOH} + 2\mathrm{H} + + 2\mathrm{e^-} \leftrightarrow \mathrm{HCHO} + \mathrm{H_2O} \qquad (\mathrm{pH} = 0, \mathrm{E^\circ} = +0.056)$$

$$\mathrm{HCOO^-} + 2\mathrm{H_2} + 2\mathrm{e^-} \leftrightarrow \mathrm{HCHO} + 3\mathrm{OH^-} \qquad (\mathrm{pH} = 14, \mathrm{E^\circ} = -1.070)$$

Electroless copper solutions, utilizing formaldehyde as reducing agent, employ high pH, but simple copper salts are insoluble at pH above 4 [29]. This necessitates the use of a complexing or chelating agent, which essentially allows for the formation of more complex cupric salts that are soluble at the required pH, such as ethylenediaminetetraacetic (EDTA). The electroless bath, however, is quite unstable due to formation of undesired cuprous oxides, requiring the addition of a variety of stabilizers to allow for a long-lasting stable bath and consequent uniform plating [31].

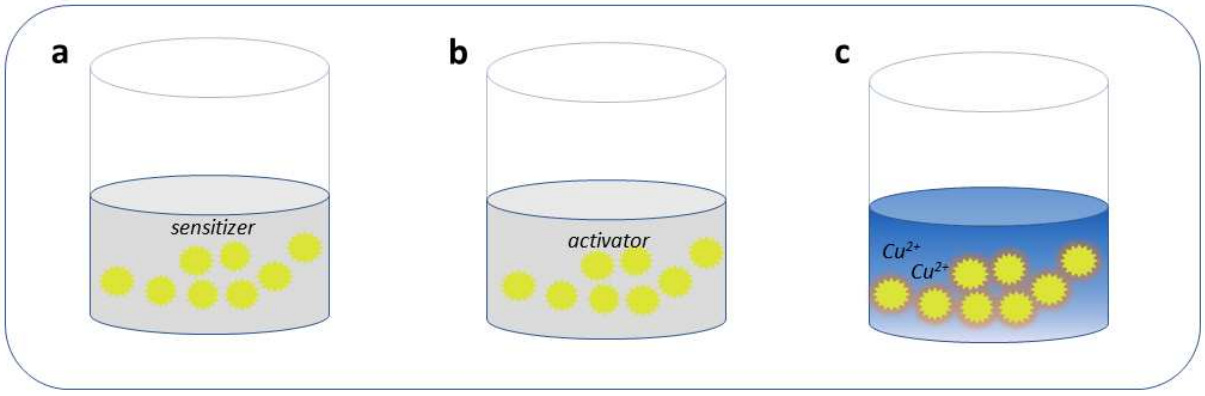

Figure 2.2. *Protocol for electroless copper plating of fabricated structures.* ***(a)*** *The structures are deposited in a sensitizer tank where stannous chloride creates adsorption sites on the surface.* ***(b)*** *Palladium chloride in the activator tank serves as a catalytic compound for the copper deposition.* ***(c)*** *Final stage of the deposition, the printed structures are deposited in the electroless copper bath, commercially provided as electroless copper A and electroless copper B. The deposition is continuous until the cuprite salts are depleted, and the solution becomes clear. Consistent shaking ensures the deposited layer is even and bubbles of hydrogen do not form on the plated surface mid-deposition.*

2.3.2 Materials and techniques in electroless plating

A protocol for the preparation, activation, and plating of the printed particles is detailed from a commercially sourced electroless copper plating kit (Caswell Electroplating). The particles were all plated at room temperature. A few adjustments are made to ensure the plating is sufficient, uniform and effective for the micron-sized particles, since the commercially available protocol is intended for larger structures. I learned that each step in the plating process is critical for ensuring defect-free plating.

To determine the most effective treatment protocol, we investigated systematic variations to the basic protocol. I vary procedures pre-deposition, during deposition with plating time and level of agitation of the bath as well as post-deposition. For pre-treatment, the particles are thoroughly cleaned using either a single twenty-minute sonication or three ten-minute cycles in acetone. This serves to remove any organic and inorganic contaminants that could potentially inhibit the plating, promoting good adhesion and a uniform coating free from defects.

The particles are then rinsed in Millipore water to remove any cleaning agent residue. They are then treated in a sensitizer tank to create adsorption sites on the particles' surface. This is followed by treatment with palladium chloride in the activation tank, making the particle surface catalytic. These steps are both preceded and accompanied by rinsing in a Millipore bath to reduce contamination.

The electroless bath consists of a copper (II) salt, formaldehyde as the reducing agent, EDTA serving as the complexing agent, and commercial stabilizers. These components are commercially provided as Electroless Copper A and Electroless Copper B. The expected plating rate and thickness is 0.5 μm per hour. The particles are deposited in the plating bath for about an hour, with consistent frequent shaking in order to control the formation of bubbles on the substrate and prevent metal deposition. We vary the level of agitation as well, ranging from light frequent agitation to systematic powerful agitations.

The bath is kept at room temperature, and once the solution is depleted, the particles are dried, and rinsed further in Millipore water. Two different post treatment protocols are also explored. The particles are either rinsed with minimal perturbation or a thorough five-minute sonication in Millipore. Before rinsing, the particles are dried to ensure the coating sets and the integrity of the plating layer is preserved. Rinsing serves to remove any residual chemicals on the surface, and thorough drying limits oxidation and contamination of the plated particles.

2.3.3 Electroless plating functionalization

This section details the results of the coating procedure on a microfabricated 20-point particle of diameter 500 μm. The fabrication of this structure, using 2PP, is described in detail in the following Section 2.4. The images in Figure 2.2 were taken using bright-field optical

microscopy (Nikon, Eclipse Ti), with a 40X Nikon S FLUOR objective, NA 0.6, pre-terminal cleaning as well as post terminal cleaning. All presented particles are treated as previously discussed, with systematic variations to explore how these affected the coating outcome. These systematic differences explore the effect of different treatment protocols.

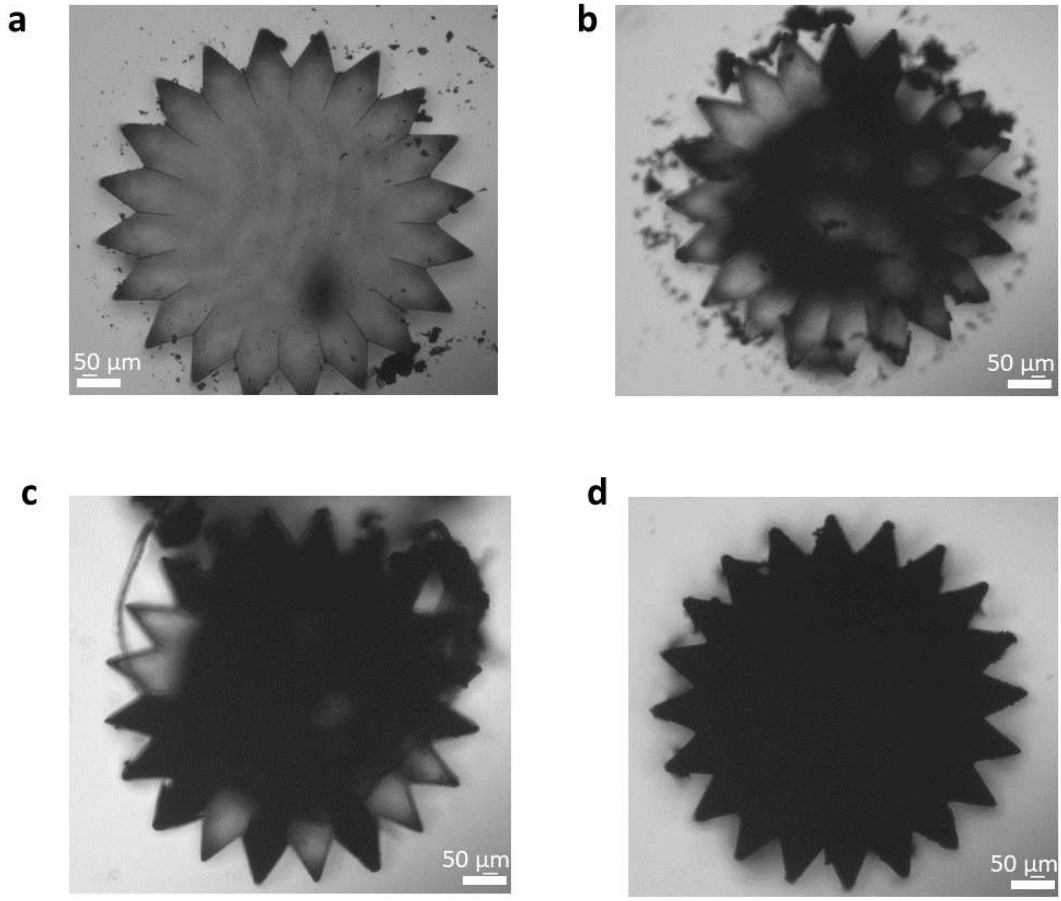

Figure 2.2. *Bright field optical microscopy images of different electroless copper plating samples with variations in pretreatment and post-treatment protocols. An unagitated sample yields a non-uniform deposition* ***(b)****. Cleaning in Millipore also yields a less effective deposition due to presence of oil and a less vigorous cleaning of the surface pre-deposition* ***(c)****. Pretreatment in acetone for longer times yields a more steadfast adherence of the deposited metal* ***(d)****. Agitation of the electroless copper plating bath also affects deposition due to a reduced occurrence of bubbles on the surface during deposition, ensuring a uniform smooth layer of deposition for sufficiently agitated samples.*

Figure 2.2a shows a sample pretreated using the idealized protocol, but post-treatment involves an intensive sonication in Millipore without the intermediate drying step. Figure 2.2b shows a sample that is left unagitated in the bath, leading to nonuniform deposition characterized by nucleated clusters around the particle. For particles cleaned with three cycles in acetone, there is uneven coverage on the surface as shown in Figure 2.2c. An initial one-cycle cleaning of acetone with a similar electroless plating time scale produces particles with good, but not excellent coverage.

From this, I develop the best experimental protocol involving three ten-minute sonication cycles in acetone, light consistent agitation in the electroless copper bath and a terminal five-minute light rinse in Millipore after drying. Generally, electroless plating until the bath is depleted yields uniformly plated structures, provided the established best experimental protocol is applied as shown in Figure 2.2d.

2.4 Structure design and fabrication

In this work, we apply 2PP to fabricate structures from the macroscale (1600 µm) down to the microscale (2 µm). In this section, we first introduce the general setup used in fabrication from the printing setup, to substrate treatment before and after printing, then more specifically discuss the printing of the large structures and the small structures.

2.4.1 Printing setup

2PP systems are typically set up as inverted microscopes, with objective lenses to focus the femtosecond laser into the desired region of photopolymerization in the photoresist. Figure 2.3 shows a typical femtosecond laser setup for TPP.

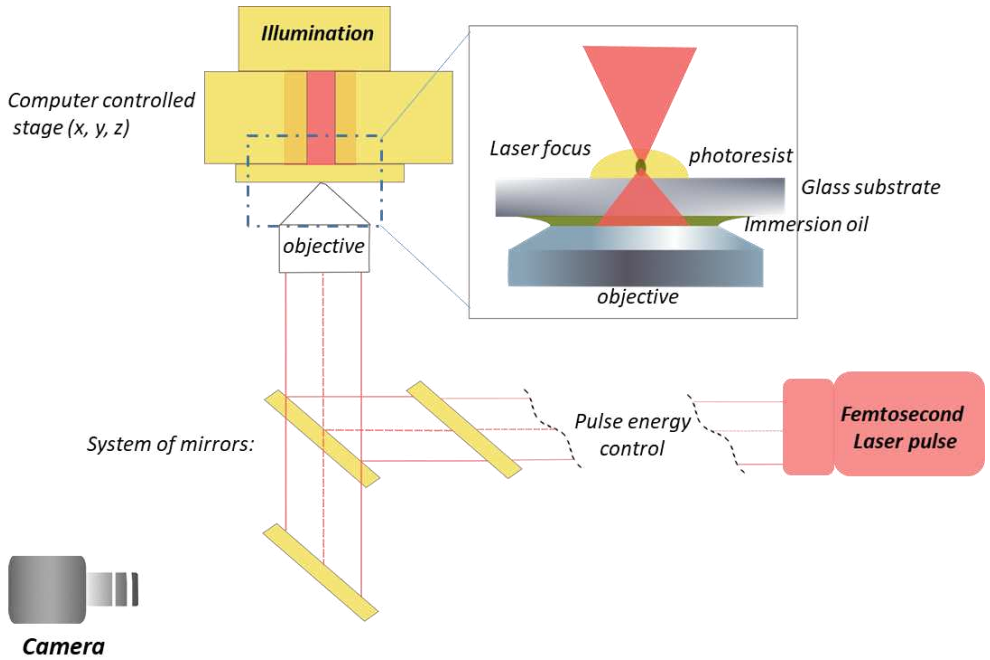

Figure 2.3. *Schematic illustration of the 2PP printing system. Inset shows the objective-substrate interface filled with the immersion oil to increase resolution of the print. The substrate is between the objective and the photoresist; the laser passes through the substrate and the immersion oil to focus on the photoresist volume (bottom-up printing). The camera images the printing process, while a system of mirrors and the pulse energy control shape, control and manipulate the beam to ensure adequate power is sent to the system for polymerization.*

The resolution and processing times of the system are determined by the optical characteristics of the objective; a higher magnification means a greater resolution, but also a smaller field of view and a longer processing time. The photoresist is applied to the prepared substrate and placed over the lens as shown in Figure 2.3. A greater magnification is necessary for smaller structures and oil immersion is necessary to increase the resolving power of the microscope. The oil replaces the air gap between the immersion objective lens and cover glass with a high refractive index medium reducing light refraction. Applying bottom-up printing with the NanoOne 1000 (UpNano), fabrication occurs through both the substrate and the immersion oil necessitating thinner substrates but also further limiting the z-axis range. Furthermore, since the print origin is taken at the substrate-photoresist interface and the system prints in the positive z-axis direction, therefore limiting the range of heights possible using a greater objective, as well as the range of possible substrates. With smaller objectives, an air interface is sufficient, and printing bigger structures is possible.

We use a commercial nano printing setup (NanoOne 1000 by UpNano gmbH) with a 40X objective (UPlanXApo, NA = 1.40 Oil, UpNano gmbH), a 20X objective (UApo N 340, NA = 0.70 W, UpNano gmbH) and 10X objective (UPlanXApo, NA = 0.40, UpNano gmbH) and commercially available resins (UpBrix, UpPhoto and UpSol, UpNano gmbH) to print our microparticles. These particles are designed using CREO Parametric, a Computer-Aided Design (CAD) software (CMT v90, Techsoft 2022 copyright). The specific printing parameters are outlined in Table 2-2.

Table 2-2. Printing parameters of each photoresist

	Input laser power	*Scanning speed*	*x-y scanning hatching size*	*z layer height*
UpPhoto	50mW	600 mm/s	4.2 µm	5 µm
UpBrix	20 mW	150 mm/s	1 µm	0.5 µm
UpSol	10mW	150 mm/s	0.15 µm	0.25 µm

2.4.2 **Substrate treatment**

The following procedure was used to prepare substrates before printing. First, a microscope coverslip ($17 \times 17 \times 3\,\mathrm{mm}^3$, Thermo Scientific) was rinsed with acetone and 1,2-polypropanol (IPA) and plasma treated. Using acetone and IPA in this cleaning protocol ensures that both organic and inorganic material are removed from the surface. An additional IPA rinse ensures the removal of acetone residue on the surface. Plasma treating the substrate further removes organic material. For the macrostructures, a solution of dextran (20 w/v %) and glucose (20w/v %) dissolved in Millipore water was spin-coated at 3000rpm for 75s on the treated substrate [32]. This layer of dextran acts as a sacrificial layer to allow the transfer of particles from the substrate. This step, shown in Figure 2.4a and necessary to recover the printed object from the substrate, was adapted from Steven van Kesteren's doctoral work [32]. For the microstructures, the dextran sacrificial layer is omitted, since the structures are applied experimentally directly on the substrate.

After printing, I follow a standard post-treatment step to get rid of any additional untreated resist. I adjust the development times and cycles based on the size and geometry of the printed structures. For UpBrix, the standard recommended procedure is immersion in PGMEA (1-methoxy-2-propylacetate, CAS 108-65-6) for 10 minutes and an additional 2-minute rinse in 2-propanol (CAS 67-63-0) [UpNano gmbH]. For UpPhoto, two to three baths in 2-propanol (CAS 67-63-0) are recommended. For UpSol, submersion in 1-propanol (CAS 71-23-8) until the excess photoresist is removed and a further rinse in 1-propanol (CAS 71-23-8) is recommended. For the macrostructures, after the post development step I submerge the substrate in Millipore water to dissolve the glucose/dextran layer and release the particles as illustrated in Figure 2.4b.

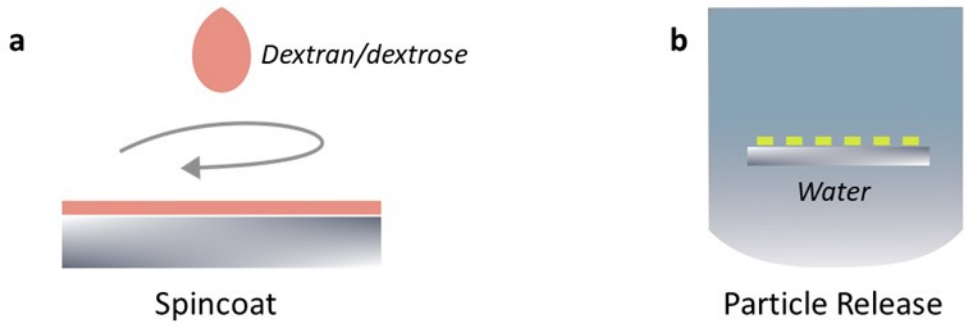

Figure 2.4. *Substrate pretreatment and posttreatment protocol. The substrate is cleaned via plasma treatment, rinsing in acetone and IPA.* ***(a)*** *Spin-coating a sacrificial layer of dextran/dextrose at 3000 rpm.* ***(b)*** *Post treatment of the substrate after printing. The substrate is deposited in a water bath to dissolve the sacrificial dextran/dextrose layer and release the printed particles.*

2.4.3 Macrostructure design and fabrication

We explore the design and fabrication of large structures using 2PP, aiming to evaluate and showcase the resolution, aspect ratio integrity and quality of the printing process. Large structures require careful design to achieve high aspect ratios and complex shapes. We explore three main designs, ranging from 50 μm to 1800 μm. I present and characterize below the different designs I performed for this thesis: gears, disks and teeth, and asymmetric walkers inspired by previous work by Dauchot [1].

2.4.3.1 Gears, disks and teeth

We print several different large structures to explore the resolution and printing quality of the 10X objective. For this, we print gears with major diameter 50 μm and 20 teeth as well as one of major diameter 500 μm which I electroplated as shown in Section 2.3.3. In addition, I designed a more complex structure with additional features: teeth and a square hole. These are simple, easy to access structures.

Figure 2.5 shows optical brightfield images, imaged using a 40X Nikon S Plan Fluor with a 0.6 numerical aperture. The structure in Figure 2.5a, referred here as teeth, is printed using UpBrix and a 40X objective. The structure's dimensions are $10\ \mu m \times 20\ \mu m \times 10\ \mu m$ with teeth that are roughly 0.5 μm. These structures exhibit true three-dimensional fabrication; even with a 10 μm height and a 20 μm length, the structure requires no additional support structure. The sharp edges are resolved to the sub-micron level as shown in Figure 2.5a. Figure 2.5b shows a sample of larger structures of diameter 50 μm, printed using UpPhoto and a 10X objective.

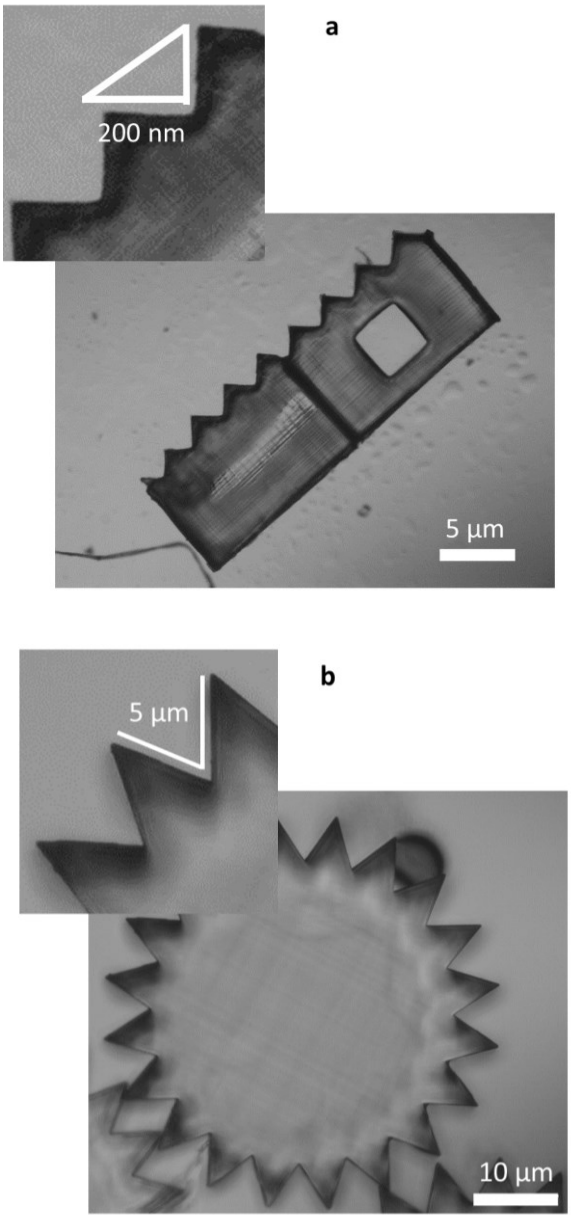

Figure 2.5. *Bright-field optical microscopy (Nikon, Eclipse Ti) images of the 2PP-printed gear and teeth structures.* ***(a)*** *Bright field top view optical image of a* $10\ \mu m \times 20\ \mu m \times 10\ \mu m$ *structure. The teeth are* $\sim 0.5\ \mu m$*. The structure is printed using UpBrix and a 40X objective. The square structure is an additional indicator of the high resolution of 2PP* ***(b)*** *Bright field top view optical image of a 50* μm *diameter 16-point gear printed using UpPhoto with a 10X objective.*

In addition to the gear and teeth structures, we also printed a “puck”: a disc with an internal channel. Although this design assisted a colleague on a different set of experiments, it nonetheless allowed me to investigate the structural stability of 3D micro-objects that present bridging structures. This puck design has a 50 μm height, featuring a 5 μm wide channel of 5 μm depth. In order to further characterize the topography of my channel, Felix Pertl and I perform AFM topography measurements in non-contact mode at a scanning rate of 0.3 Hz.

The AFM maps a 3 μm depth, and a 5 μm width, that is however, not square as designed. This is exhibited in Figure 2.6a, with the depth and width values further supporting the printing’s capability for highly resolved structures. While the print exhibited strong performance in terms of external structure and resolution, the depth of the fabricated channels revealed slight inconsistencies. This could be attributed to some convolution due to the size of the AFM scanning tip Finally, I imaged the structures with Samuel Hajek using an SEM, as shown in Figure 2.6b, providing an intuitive idea of the printed structures.

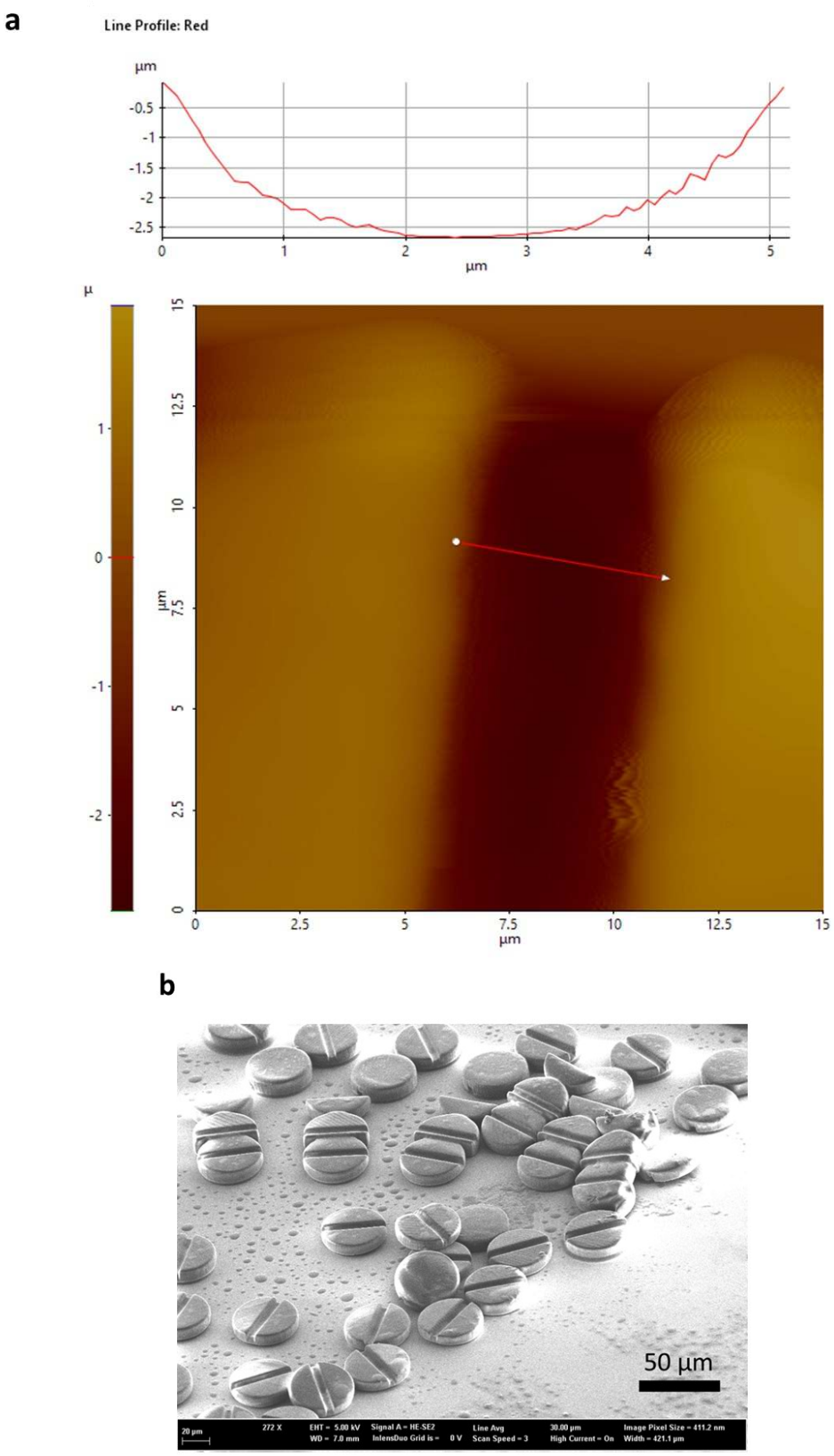

Figure 2.6. *SEM and AFM images characterizing the printed 'puck'* ***(a)*** *AFM image of the 'puck' channel. The attached line profile shows a curved profile, rather than the designed square channel* ***(b)*** *SEM images of 2PP printed disks of diameter 50 µm with a 5 µm wide, 5 µm deep channel in the center of the cylinder.*

2.4.3.2 **Walkers**

I next design a walker, so named due to their desired functionality: as a simple structure to investigate motion, or a random walk on a vibrating surface. The walkers exhibit a structural asymmetry, with one leg shorter than the other. The walker structure, shown in Figure 2.7, was printed with a length of 800 µm, a height of 215 µm and each leg 300 µm. This design leveraged the ability of 2PP to maintain fine structural details and consistent aspect ratios in simple geometry. Conveniently, the resin presents autofluorescence, allowing us to characterize our structures with confocal microscopy. 3D reconstructions of millimetric walkers in Figure 2.7 exhibit well-defined edges.

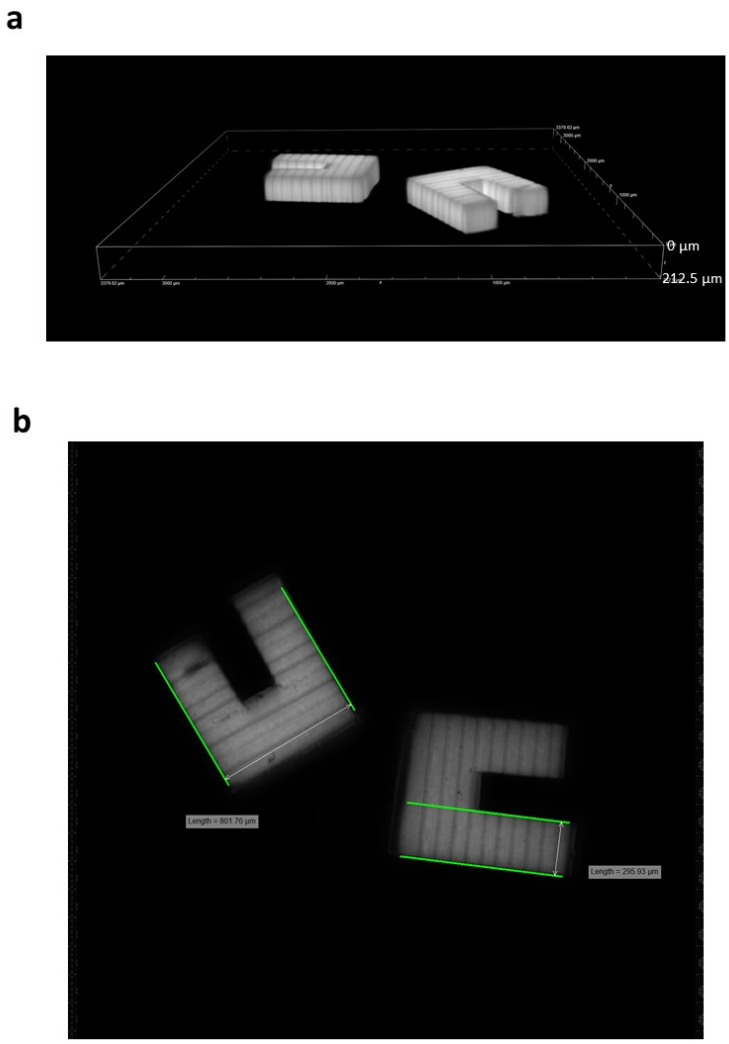

Figure 2.7 *Confocal image of the walkers, fabricated using UpPhoto with a 10X objective.* ***(a)*** *Side view of the printed walkers, highlighting the height of the structure. We design the walker to have a height of 215 µm, and observe the height of the fabricated walker to be 212.5 µm, with very well resolved edges* ***(b)*** *Additional confocal image of the structure, top view indicating the length and width of the structure as well as the asymmetrical design.*

2.4.3.3 **Asymmetric particles**

An additional design are asymmetric particles, inspired by previous work by the group of Dauchot where polar asymmetric particles walked on a vibrating surface [1]. I aim to reproduce comparable results by 3D printing the particles. Unlike Dauchot's particles which had a diameter of 4mm and a 2mm height, we print particles with a diameter of 900 µm and a height of 450 µm with an off-center leg of height 100 µm and a tapered 300 µm leg attached. We maintain the design of a slightly narrower 400 µm leg on the diametrically opposite side.

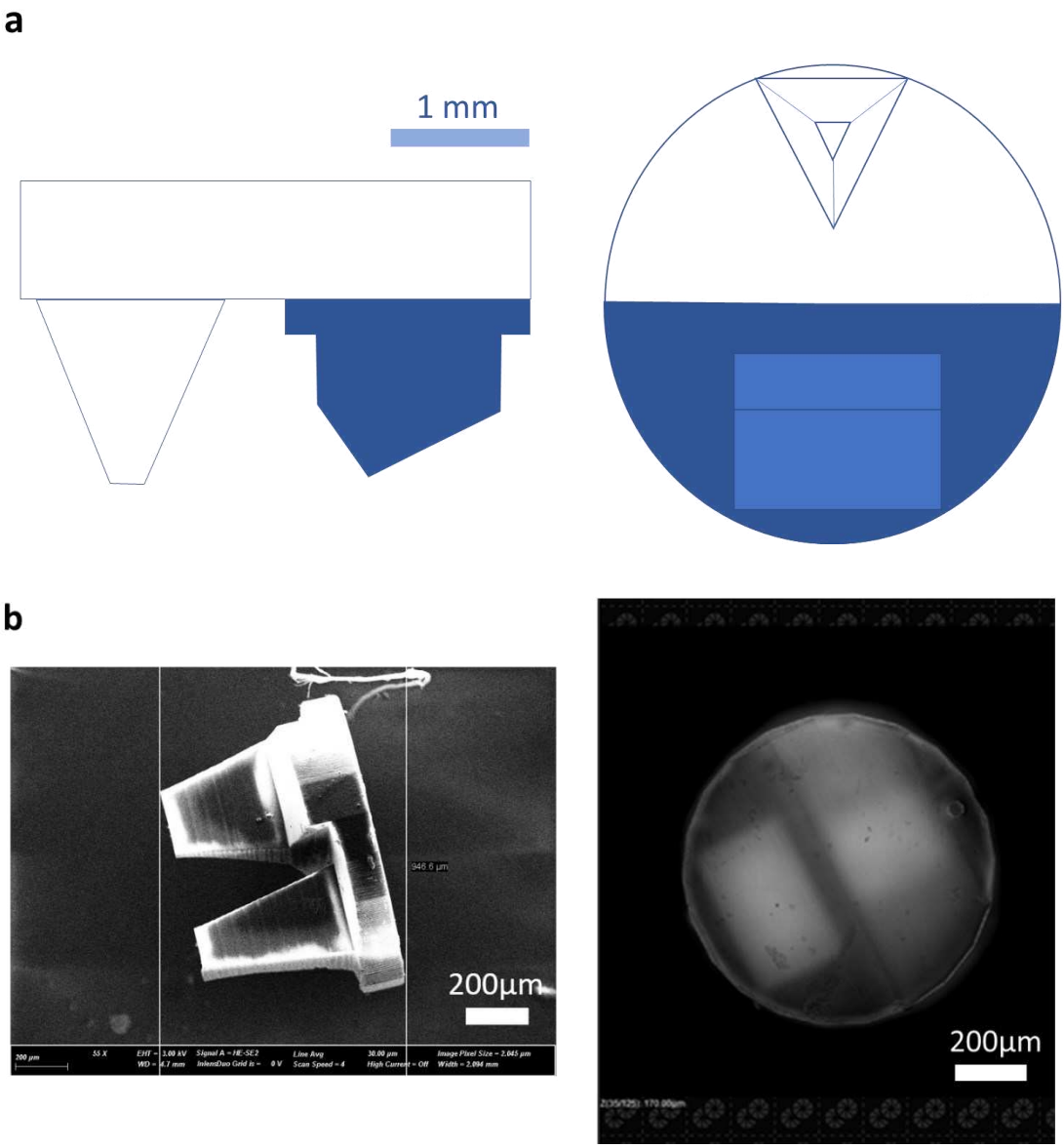

Figure 2.8. *Comparison of the first iteration of the printed asymmetrical particle to the reference Dauchot particle.* ***(a)*** *Side and top view illustration of the Dauchot particle. The blue section is made of rubber, while the clear part is copper. The disk has a 4mm diameter, while the legs are 2mm long* ***(b)*** *SEM image of the side view illustration of the printed asymmetrical particle and the top view confocal image of the printed asymmetrical particle. The printed particle has a diameter of 800 µm and a 500 µm height.*

Our proposed design, and the comparison to the original design by Dauchot, is presented in Figure 2.8. A more detailed view of my proposed walker is presented on Figure 2.9 - notably presenting a 3D reconstruction from confocal microscopy and SEM.

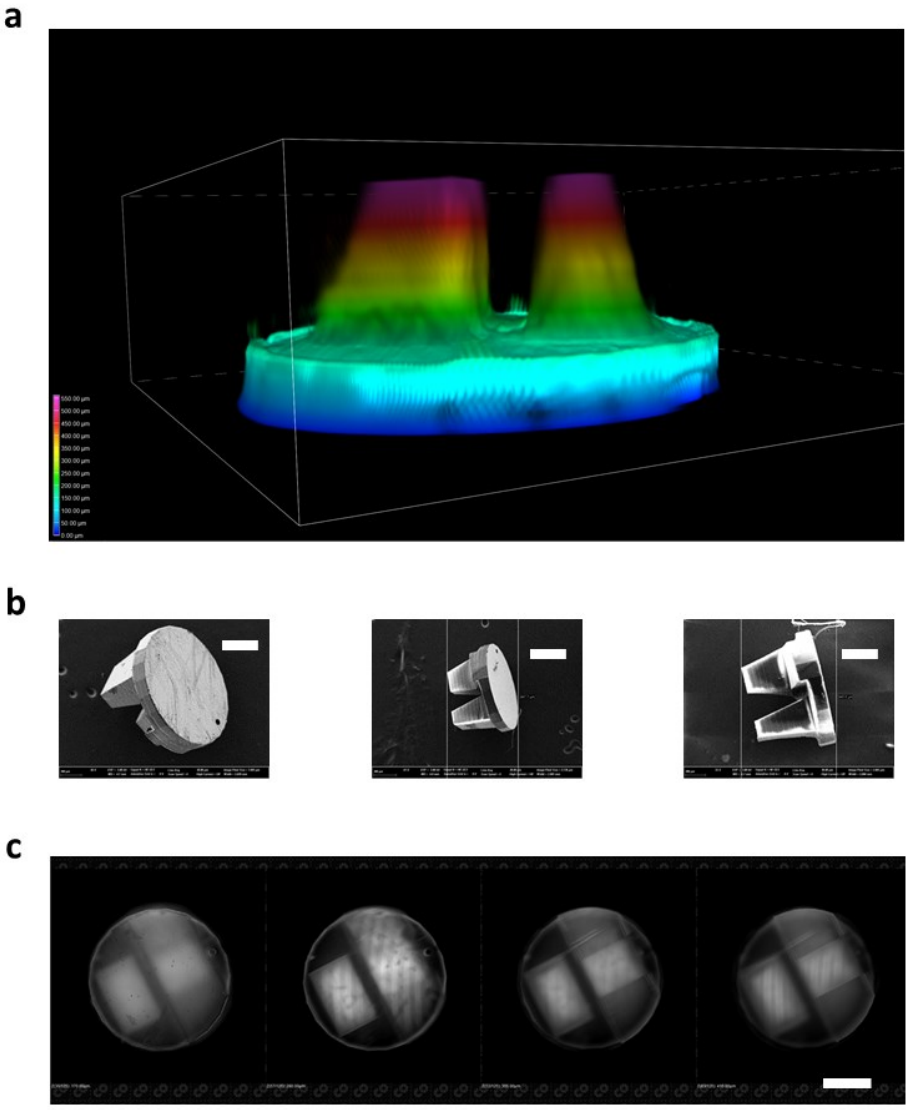

Figure 2.9. *Confocal microscope and SEM images of the printed asymmetrical particle.* ***(a)*** *Confocal image of the asymmetrical particle showing the z axis evolution of the print. There is structural integrity in the performance of the print, as indicated by the scale of the height as well as the sharp edges in the image. However, the resolution of the confocal image does not show the additional step in the leg as indicated in the different imaged particles* ***(b)*** *SEM images of the asymmetrical particle. This image also further underscores the resolution of the prints, particularly even with the 10X objective for larger structures. The bars indicate a 200 µm length* ***(c)*** *Confocal image of the top view of the printed asymmetrical particle*

However, our design is unstable under vibration causing the particles to flip. To resolve this design flaw, I redesigned the asymmetrical particle to be mirrored along the z-axis, aiming to allow walking even after flipping of the particle. This modification improved the particle's stability and introduced additional complexity to the particle, allowing further observation of print quality. Figure 2.10 showcases these particles, printed using UpBrix at 20X. Figure 2.10b

shows SEM images of the printed particle, with an overall height of 1800 µm and a diameter of 600 µm; an aspect ratio of 2:3. However, this change of design remained insufficient to achieve stable walking.

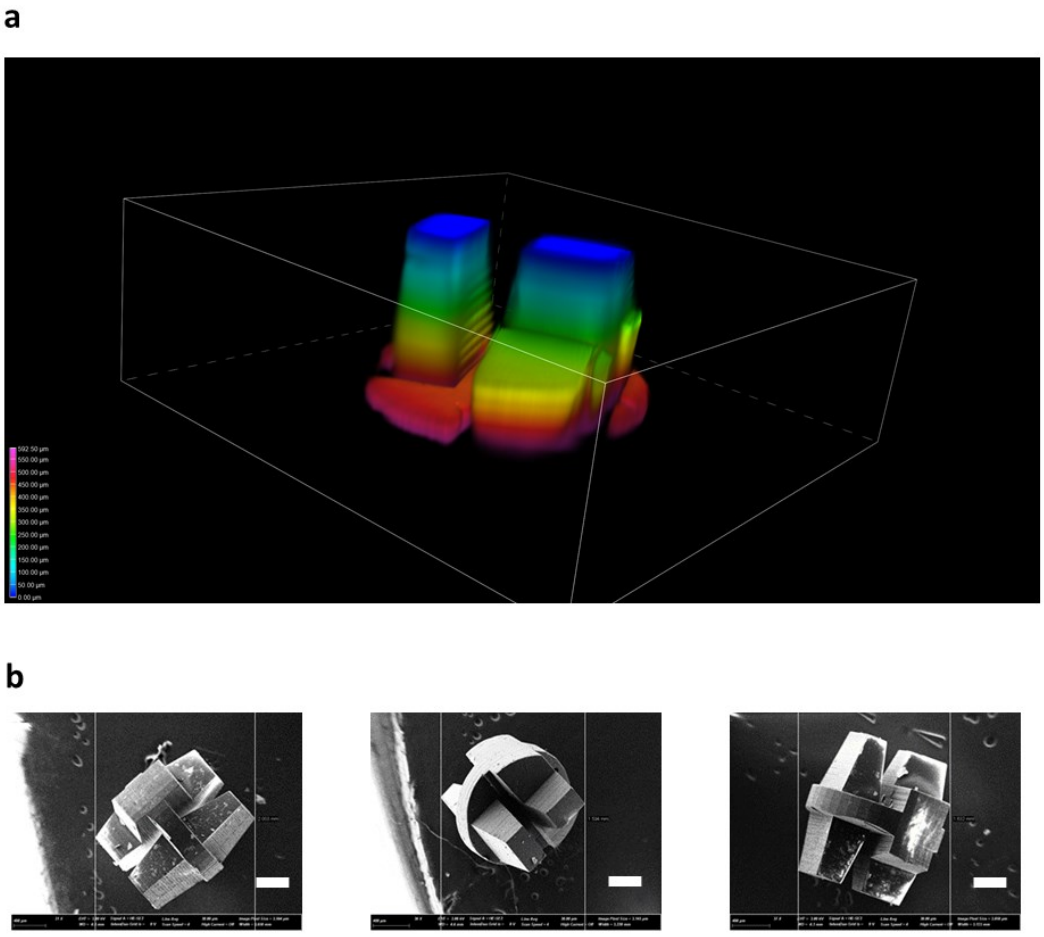

Figure 2.10. *Double-sided asymmetrical particles* ***(a)*** *Confocal images of redesigned double-sided asymmetrical particle* ***(b)*** *SEM image of the redesigned asymmetrical particle, showing well-defined edges and <2 µm resolution. The bars indicate a 300 µm length.*

2.4.4 **Microstructure design and fabrication**

While the previous part was focused on the design of large (millimetric) 3D objects using 2PP in nano printing, the section below aims at fabricating a sensor to quantify the forces exerted by a single colloidal micro swimmer or swimming bacteria. To this end, I propose to devise a beam, which will deflect "sufficiently" under application of a force of order 0.1 pN. I will show below that this requires the investigation of 3D printing at considerably smaller scales than investigated in Section 2.4.3; down to the µm or below.

The development and characterization of this microsensor constitutes the second part of my thesis. Let me first introduce the fundamental concepts that I need to devise and parameterize the microsensor.

2.4.4.1 Theoretical parameters

Under application of a force F at its tip, an anchored elastic beam deflects. The deflection δ of the beam of length L under the force F is given by:

$$\delta_{max} = \frac{FL^3}{3EI} \tag{2.4.1}$$

where E is the Young's modulus and I is the moment of inertia.

We estimate the typical force exerted by a swimming bacterium or an active colloid to $F = 0.1$ pN. We perform Atomic Force Microscopy (AFM) characterization of the photoresist to determine the Young's modulus, E. We use UpSol (UpNano gmbH), chosen for its ability to support overhang structures, a characteristic that is essential for creating freestanding beams. We determine an average Young's modulus value of $E = 2.5$ GPa. This value was comparable with data from a similar material, SZ8020 [33], provided for comparison from the manufacturer ($E = 0.6 - 2.8$ GPa).

We consider the moment of inertia, I, of a rectangular beam:

$$I = \frac{bh^3}{12} \tag{2.4.2}$$

where h is the thickness of the beam and b is the width of the beam as shown in Figure 2.11.

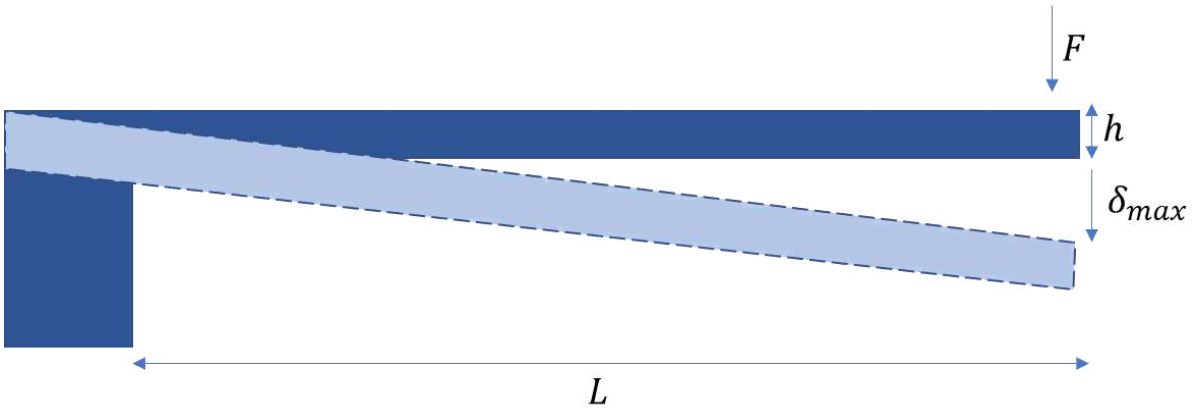

Figure 2.11. *Scheme showcasing the parameters and dimensions to be considered in beam design*

The minimum printable thickness of the beam was constrained by the capabilities of the nano printer. To ensure the beam's structural integrity while maintaining high sensitivity, the thickness was optimized based on the printer's resolution and the required mechanical stability.

Assuming a maximum beam deflection, $\delta_{max} = 5$ µm, and the above order of magnitude of applied force and Young's modulus, we obtain the moment of inertia of the beams $I = 3.3 \times 10^{-24}$ m^4. We propose a beam length, $L = 250$ µm, $b = 5$ µm, $h = 2$ µm to get this

value and account for the limits of the structure's stability under small force applications and the maximum allowable overhang.

Following those estimations, we designed and 3D printed our beam, which is characterized and discussed below.

2.4.4.2 Structure design and fabrication

Figure 2.12 shows the finalized beam structure design. In order to reduce sagging or collapse, I applied a small voxel size, used a high magnification objective, a layer size of 0.1 µm and an offset stitching during printing.

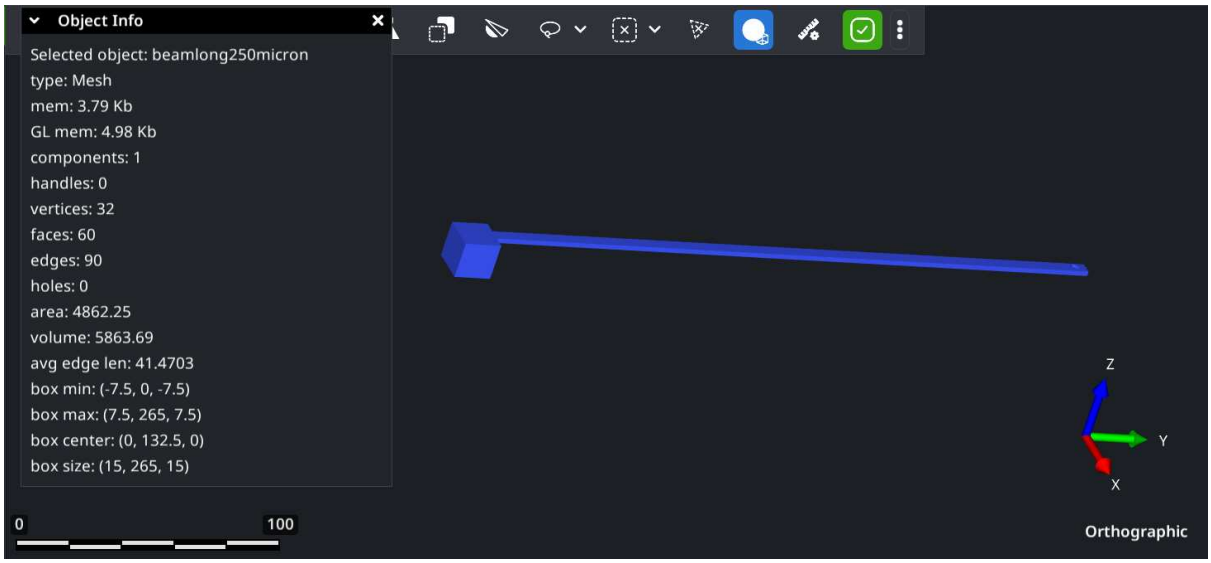

Figure 2.12. *Finalized beam structure design. The design was optimized to meet the length, thickness and modulus boundary conditions. An additional hole is added at the end of the beam, to ensure the colloid is sufficiently constrained at the position to determine deflection.*

The array of printed beams in Figure 2.13a demonstrates the precision and accuracy of the printing process. The printed beams show well-defined, consistent dimensions across the array, with measured lengths and widths falling within the designed tolerances. For example, the printed beams exhibit dimensions ranging from 2 µm to 250 µm, as marked in Figure 2.13. The radius of the circular 'colloid receptacle' is measured to be 1.99 µm, with the designed structure 2 µm, showcasing the high-resolution capability of the printing, even when producing long and thin structures. However, this brightfield does not offer insights into the 3D evolution of the printed structure to comment on whether the structures sag. To this end, I applied 3D confocal microscopy to visualize the 3D shape of the structures.

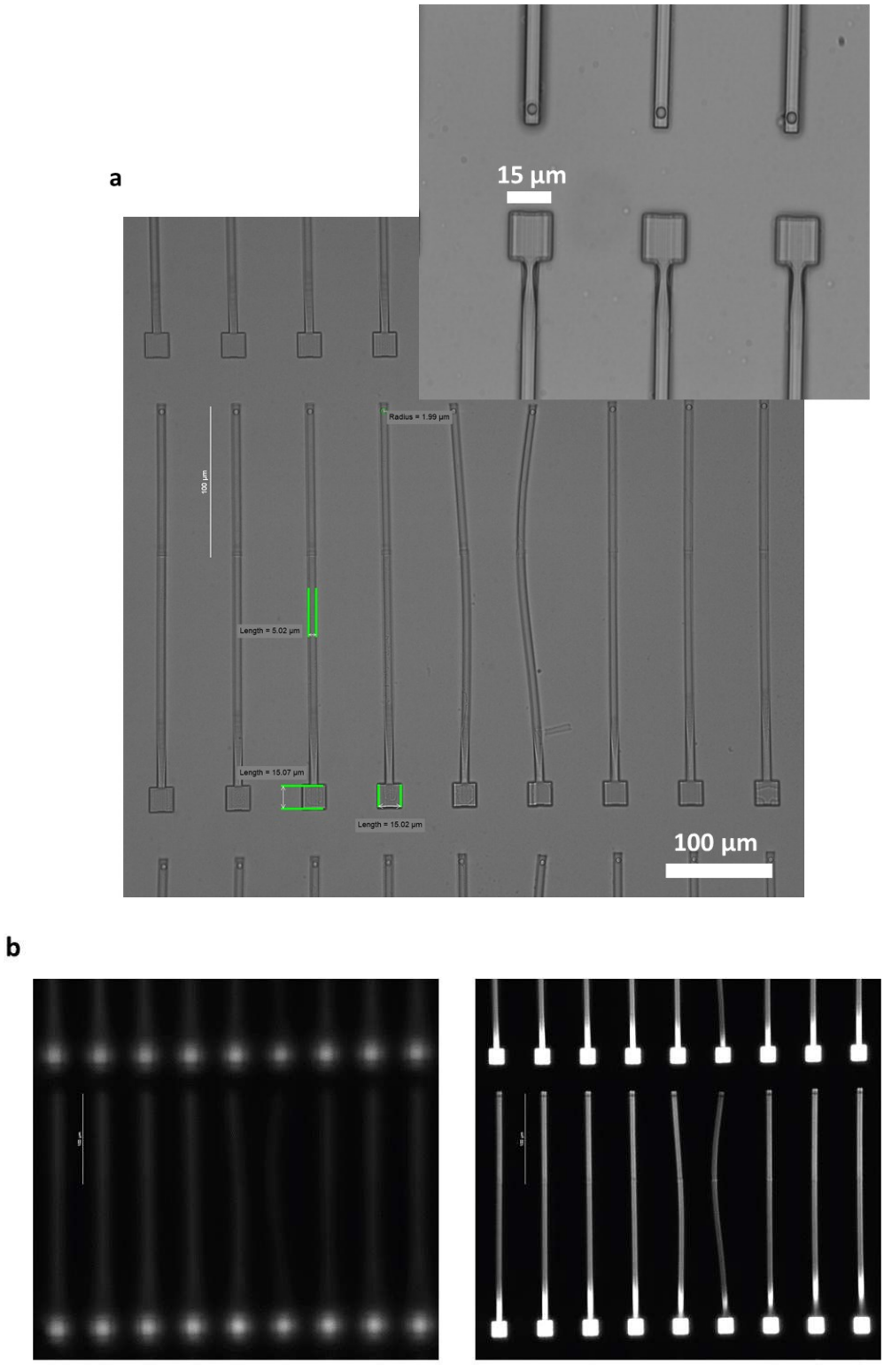

Figure 2.13. *Confocal images of the array of printed beams* ***(a)*** *Well-defined, consistent dimensions across the array, with measured lengths and widths falling within the designed tolerances. The width of the beams is recorded as 5.02 µm compared to the designed 5 µm, the diameter of the colloid receptacle is 1.99 µm compared to the 2 µm of the design. The length of the beam support is 15.02 - 15.07 µm to the designed 15 µm.* ***(b)*** *Confocal images of the evolution in the z axis. The image on the left is taken at 0 µm and the right image is taken at 15 µm, showcasing the consistency in the height profile of the printed structures.*

Printing overhangs without sagging is challenging in microfabrication due to gravity and the lack of immediate support during the curing process. When printing thin beams or suspended structures, sagging can distort the geometry, compromising precision and functional performance. To overcome this, I used a specialized sol-gel resin (UpSol, UpNano gmbH), whose formulation as a gel ensures stability and rigidity during polymerization, even in unsupported sections. Additionally, I adjusted the print path and curing sequence, ensuring that the material was stabilized incrementally to prevent sagging. This resulted in beams printed uniformly along the beam length that should behave predictably under the applied forces in colloidal experiments, where even slight variations in beam geometry could significantly impact force measurement accuracy.

Still, it is worth noting that some beams exhibit minor deformation in the form of slight curvature, which is likely caused by capillary forces during the development stage. Since post-treatment involves submersion in 1,2-isopropyl alcohol (IPA) to remove any undeveloped photoresist, the curvature seen in certain beams aligns with the expected behavior when solvent-induced forces interact with these delicate structures. This phenomenon underscores the need for controlled solvent exchange processes to minimize deformation post-printing.

From the confocal images in Figure 2.13b, Figure 2.14a and Figure 2.14b, slight bending at the connection point between the support and the thin beam in the structures raises another key question of whether the low part is tethered to the substrate as this would impact the desired deflection as a measure of applied forces. Though we observe the slight horizontal curvature in some of the beams, suggesting a free-standing beam not tethered to the substrate, this curvature does not appear in all the beams. Additionally, it is unclear whether the deflection itself is due to capillary forces or due to gravity, causing the structures to sag under their own weight.

Based on the scale of the printed structures and their rigidity, it appears, qualitatively, that gravity alone would not account for the observed sagging in most cases. I speculate that the sagging that we observe is also likely caused by capillary forces during the IPA development stage, due to the small scale of the beams and the high rigidity imparted by the resin. To clarify this aspect, I consider two paths – to test the beams as they are, using a theoretical and an experimental approach, or design a beam with two supports. If the beam was simply supported at two ends for a uniform material distribution, I predict that the weight of the beam would create a bending moment at the center. If the beam is subjected to a force equivalent to its own weight, and we assume the second half of the beam acts as a point load at the end of the first half, the deflection at the center of the beam can be estimated using the relation for a beam under a point load at its center. To this end, I propose to design and fabricate a structure with two supports, using a similar mathematical treatment as the design of the printed beams. However, as the outlook and perspectives section describes, I focused only on testing the already printed beams. This is non-trivial for the eventual application of the printed structures as potential force microsensors.

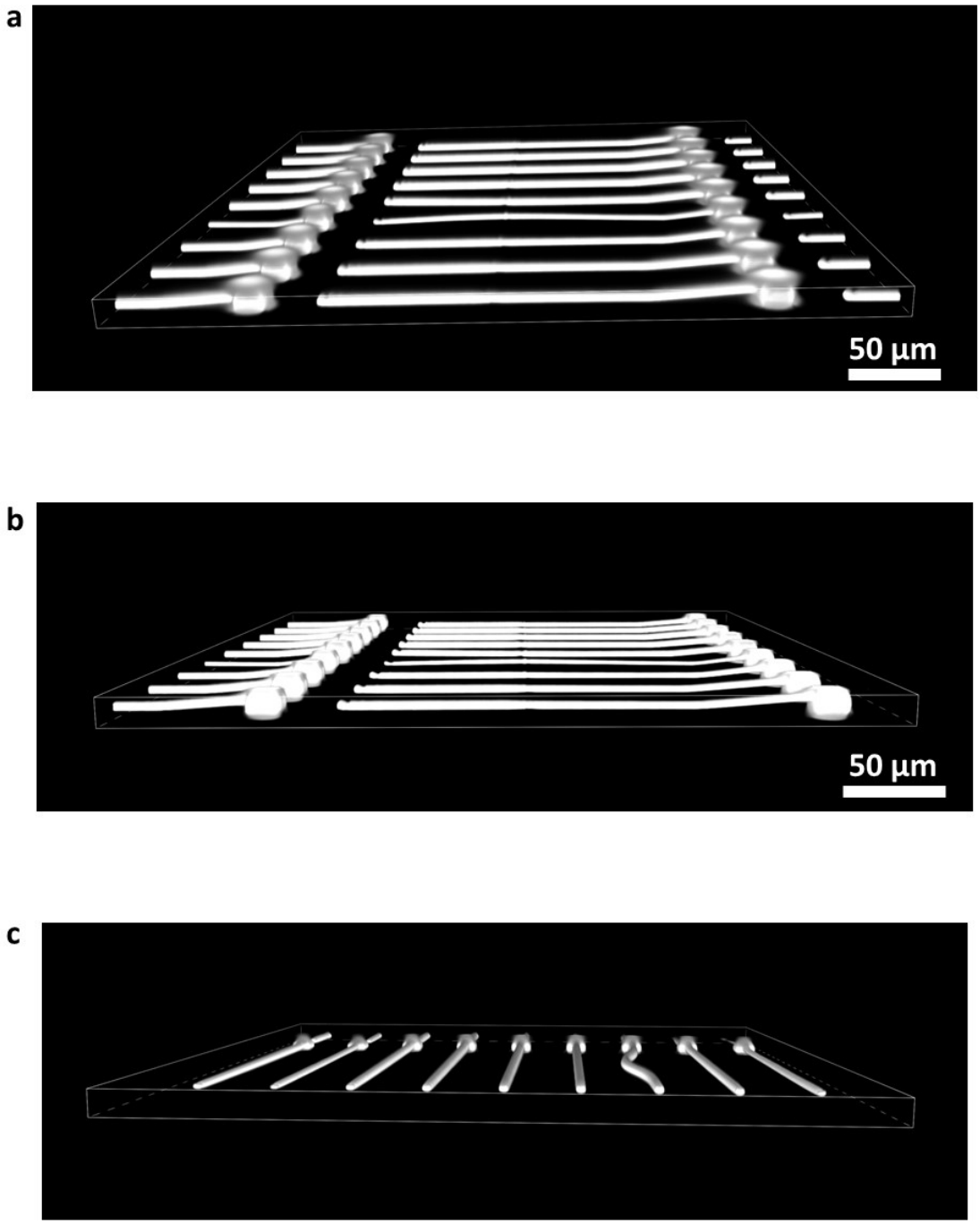

Figure 2.14. *Confocal fluorescent images of the printed arrays. UpSol is fluorescent, allowing the mapping of the printed structures to characterize the exact beam shape in the absence of any colloidal force, to test the veracity of the microsensor design.* ***(a)*** *Sample 1; showing the lack of contact of the beam with the substrate surface.* ***(b)*** *Sample 2; showing the consistency in the print on the z axis. The brightness of all the structures in the array are consistent, indicating a highly resolved and structural integrity of the print. Note the initial curve of the beam, highlighting a deflection of the printed structure post-development.* ***(c)*** *Imaged deformation of the beam presumably due to the interaction of the print with the IPA.*

2.5 Conclusion

This chapter offers an example of how the convergence of 3D nano printing technologies, specifically 2PP, and functionalization of printed structures, particularly electroless plating, can be leveraged in creating functional microstructures, hereby a millimetric walker or a micrometric force sensor. We introduce the general setup used in fabrication from the printing setup, to substrate treatment before and after printing and more specifically discuss the printing of structures ranging from the macroscale to the microscale. We further studied and developed a working electroless plating protocol as I originally intended to apply electric control to the walker in addition to acoustic vibrations. Copper plating offers a satisfactory uniform plating of intricately designed micron scale non-conducting particles. It is also a simple ready-made quick solution for creating conductive surfaces on microfabricated particles. 2PP offers an efficient bottom-up approach to microfabrication, with control over structure, size and functionality.

We explore the design and printing of large-scale structures in the range of $50 - 2000\ \mu m$, specifically the asymmetric particle, developing the structural design to counter the issue of stability. This offers insight into the resolution capabilities of the 10X and 20X objectives, as well as the performance of UpBrix and UpPhoto photoresists (UpNano gmbH). Here, we showcase a nanometric resolution even for macroscale structures.

We also explore the design of microstructures in the range of $2 - 15\ \mu m$ using UpSol photoresist (UpNano gmbH) and characterize the resolution and structural integrity of the printed structures. We design the structures to apply the principle of beam deflection to investigate the potential for colloidal force microsensors. Despite the high aspect ratio, UpSol performs sufficiently for the fabrication of the microbeam.

For future work, the printed asymmetric particles could be experimentally examined, attempting to establish whether it is the material that offers the dynamics of the particle, or whether the structural asymmetry is the property responsible for the observed motion. Additionally, the beam design could be enhanced to ensure the structures maintain structural integrity even post-development. We plan to investigate the interaction of the beams with colloidal particles to establish whether the design of the beams is appropriate for use as a colloidal force sensor.

3 Outlook and perspectives

Towards the end of this work, I aimed to develop printed microbeams that could reliably deflect under the weight of colloids, enabling accurate characterization of colloidal forces. However, even in the absence of colloids, the beams exhibited noticeable deflection, raising questions about whether their performance could be effective for the intended application. To address this, I made efforts to characterize this behavior in order to improve the structures. This section explores the theoretical considerations, the experimental approaches and the challenges encountered, and the proposed approaches for future work.

3.1 Theoretical Considerations: Gravitational Effects on Beam Deflection

One of the key theoretical approaches to understanding the observed deflection was estimating the center of mass (COM) of the beam system. To estimate the center of mass (COM) of the beam system, I treat it as a composite object consisting of two parts: the cubic support slab ($15\,\mu m \times 15\,\mu m \times 15\,\mu m$) and the thin rectangular beam ($250\,\mu m \times 5\,\mu m \times 2\,\mu m$). Assuming relative masses based on volume, I calculate the weighted average of the positions of the individual centers of mass to be 59.6 μm from the start of the support. This COM position, relatively close to the fixed end, suggests that much of the beam's weight is concentrated near its base.

From a mechanical standpoint, the beam can be approximated as a cantilever under uniform gravitational loading. The maximum bending moment occurs at the fixed support, and the deflection is most pronounced near this point. This analysis aligns well with the observed sagging seen in confocal imaging, which shows deflection concentrated near the support. The high length-to-thickness ratio of the beam further supports this, making the structure particularly prone to bending under even minor forces. While the calculated COM and theoretical predictions strongly suggest that gravity is the primary cause of the sagging, other potential influences, such as residual stresses from the fabrication process, cannot be ruled out. These effects could contribute to the observed deflection, particularly along the free end of the beam. I then explored some experimental approaches to characterize this sagging behavior.

3.2 Proposed Measurements for Characterizing Beam Behavior

Although functional beams were not achieved in this work, I explore several experimental methods to isolate and quantify the contributions of gravitational and other effects to beam deflection. One potential approach is to use atomic force microscopy (AFM) to measure beam stiffness and deflection under controlled loading conditions. The AFM's precise force application capabilities would allow for a direct comparison of the observed deflection with theoretical predictions. However, due to time constraints and unavailability of trained resources, I was unable to pursue this approach.

Another promising approach is optical trapping, which could be used to apply controlled forces at specific points along the beam. To experimentally determine beam deflection, I

planned to use an optical trap to apply controlled forces to the printed microbeams. The colloids would be introduced near the beams within a confined environment, created using double-sided tape and a cover slip, ensuring that the particles stayed localized for precise manipulation. I prepared samples for an optical characterization of these beams as illustrated in Figure 3.1. By using the optical trap to apply a known force at specific points along the beam, I could monitor the deflection using high-resolution confocal microscopy. This would allow for accurate measurement of the beam's response to the applied force, enabling a comparison between experimental results and theoretical predictions of beam deflection.

Additionally, force calibration of the optical trap would provide a clear relationship between laser power and force applied to the colloid, ensuring precise control over the experimental conditions. However, despite the promising setup, several practical challenges arose during the preparation and execution of the protocol.

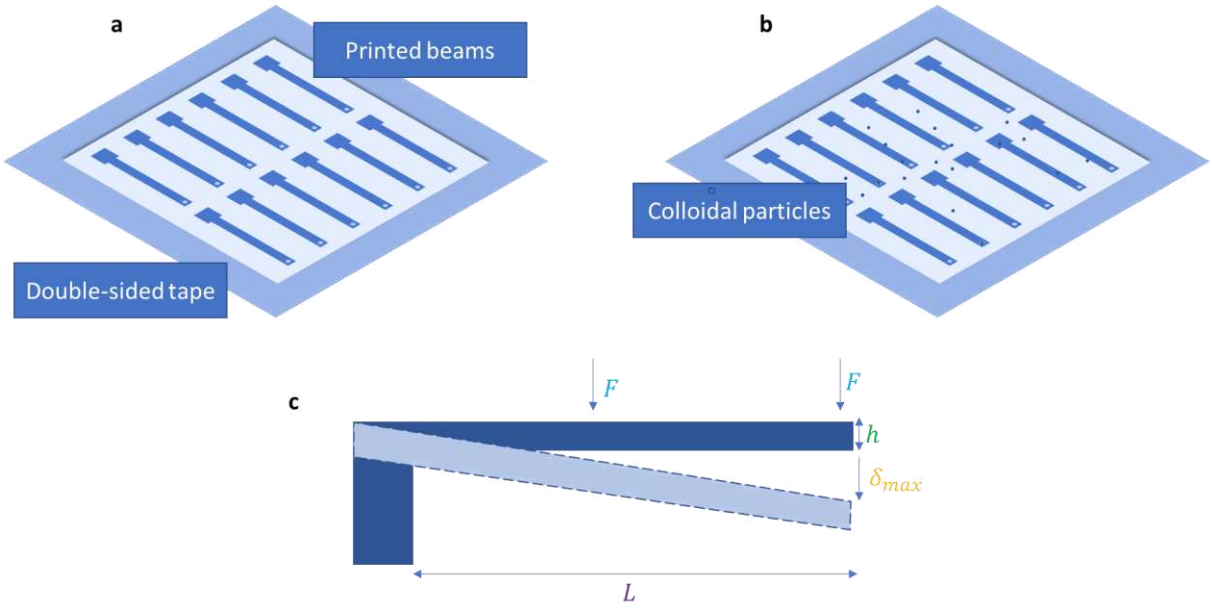

Figure 3.1. *Schematic of attempted process to determine deflection of printed microbeams. The light blue sections in* ***(a)*** *and* ***(b)*** *indicate the substrate, while the darker blue shows the double-sided tape to confine the colloidal suspension.* ***(a)*** *Applying double-sided tape to confine the beams and colloids* ***(b)*** *Colloids introduced on substrate with beams; depending on where the colloids land, I can either apply deflection calculations for a load in the middle or a load at the end of the beam* ***(c)*** *Expected deflection to observe, depending on the point of interaction of colloid and beam*

3.3 Challenges and future directions

While these experimental approaches offer promising avenues for characterizing beam behavior, there are practical challenges to their implementation. Printing large arrays of beams with consistent dimensions and mechanical properties requires time-intensive

processes, particularly when using a high-magnification objective (e.g., 40×) for precision printing. Additionally, ensuring proper confinement of colloids on the substrate, as illustrated in Figure 3.1, proved difficult due to the challenges of working with microstructures on high-precision optical glass substrates. During the sample preparation process, the fragile substrate often cracked due to the pressure applied while placing the sealing tape and placing the cover slip. While the double-sided tape's height was sufficient to prevent direct contact between the cover slip and the beams, the fragility of the substrate caused it to fail, preventing successful confinement of the colloids and compromised the integrity of the setup, making it difficult to achieve reproducible results. Additionally, the delicate nature of the beams required careful handling, and even minor misalignments during setup often led to further structural failures, preventing progress in the optical trap experiments. These challenges underscored the need for improvements in sample preparation and beam design to overcome fragility and ensure the success of future experiments.

Ultimately, understanding the mechanisms underlying beam deflection is necessary for optimizing the design and fabrication of microscale structures for applications in colloidal sensing and force measurement. While theoretical analysis of the COM provided strong evidence that the observed deflection is consistent with gravitational effects near the support, practical challenges in sample preparation, including structural fragility and difficulties in confining the colloids, prevented further validation of this hypothesis. Future work could focus on optimizing beam designs for improved structural robustness and reproducibility. Advanced experimental methods, such as AFM-based mechanical testing and optical trapping, could provide definitive insights into the factors contributing to beam deflection. By addressing these challenges, it will be possible to produce microscale beams capable of reliable deflection for colloidal sensing applications.

References

[1] J. Deseigne, S. Léonard, O. Dauchot, and H. Chaté, “Vibrated polar disks: spontaneous motion, binary collisions, and collective dynamics,” *Soft Matter*, vol. 8, no. 20, p. 5629, 2012, doi: 10.1039/c2sm25186h.

[2] A. Kudrolli, G. Lumay, D. Volfson, and L. S. Tsimring, “Swarming and Swirling in Self-Propelled Polar Granular Rods,” *Phys. Rev. Lett.*, vol. 100, no. 5, p. 058001, Feb. 2008, doi: 10.1103/PhysRevLett.100.058001.

[3] V. Narayan, S. Ramaswamy, and N. Menon, “Long-Lived Giant Number Fluctuations in a Swarming Granular Nematic,” *Science*, vol. 317, no. 5834, pp. 105–108, Jul. 2007, doi: 10.1126/science.1140414.

[4] Y. Couder, S. Protière, E. Fort, and A. Boudaoud, “Walking and orbiting droplets,” *Nature*, vol. 437, no. 7056, pp. 208–208, Sep. 2005, doi: 10.1038/437208a.

[5] D. Grober, I. Palaia, M. C. Uçar, E. Hannezo, A. Šarić, and J. Palacci, “Unconventional colloidal aggregation in chiral bacterial baths,” *Nat. Phys.*, vol. 19, no. 11, pp. 1680–1688, Nov. 2023, doi: 10.1038/s41567-023-02136-x.

[6] G. E. Uhlenbeck and L. S. Ornstein, “On the Theory of the Brownian Motion,” *Phys. Rev.*, vol. 36, no. 5, pp. 823–841, Sep. 1930, doi: 10.1103/PhysRev.36.823.

[7] S. Chandrasekhar, “Stochastic Problems in Physics and Astronomy,” *Rev. Mod. Phys.*, vol. 15, no. 1, pp. 1–89, Jan. 1943, doi: 10.1103/RevModPhys.15.1.

[8] M. C. Wang and G. E. Uhlenbeck, “On the Theory of the Brownian Motion II,” *Rev. Mod. Phys.*, vol. 17, no. 2–3, pp. 323–342, Apr. 1945, doi: 10.1103/RevModPhys.17.323.

[9] R. J. Hunter, *Foundations of colloid science*, 2. ed., Reprinted. Oxford: Oxford Univ. Press, 2009.

[10] A. V. Oppenheim, A. S. Willsky, and S. H. Nawab, *Signals & systems*, 2nd ed. in Prentice-Hall signal processing series. Upper Saddle River, N.J: Prentice Hall, 1997.

[11] M. A. B. Andrade, “Design of Single-Axis Acoustic Levitators,” in *Acoustic Levitation*, D. Zang, Ed., Singapore: Springer Singapore, 2020, pp. 27–55. doi: 10.1007/978-981-32-9065-5_3.

[12] D. Kleppner and R. J. Kolenkow, *An introduction to mechanics*, 2nd ed. Cambridge: Cambridge university press, 2014.

[13] P. A. Tipler and G. Mosca, *Physics for scientists and engineers: standard*, 6th ed. New York, NY: W.H. Freeman, 2008.

[14] H. Goldstein, C. Poole, and J. Safko, “Classical mechanics, 3rd edn San Francisco,” 2002.

[15] J.-P. Bouchaud and A. Georges, “Anomalous diffusion in disordered media: Statistical mechanisms, models and physical applications,” *Physics Reports*, vol. 195, no. 4–5, pp. 127–293, Nov. 1990, doi: 10.1016/0370-1573(90)90099-N.

[16] R. Metzler and J. Klafter, “The random walk’s guide to anomalous diffusion: a fractional dynamics approach,” *Physics Reports*, vol. 339, no. 1, pp. 1–77, Dec. 2000, doi: 10.1016/S0370-1573(00)00070-3.

[17] A. Einstein, “Über die von der molekularkinetischen Theorie der Wärme geforderte Bewegung von in ruhenden Flüssigkeiten suspendierten Teilchen,” *Annalen der Physik*, vol. 322, no. 8, pp. 549–560, Jan. 1905, doi: 10.1002/andp.19053220806.

[18] R. Kubo, “The fluctuation-dissipation theorem”.

[19] M. P. Allen and D. J. Tildesley, *Computer Simulation of Liquids*. in Computer Simulation of Liquids. Clarendon Press, 1989. [Online]. Available: https://books.google.at/books?id=O32VXB9e5P4C

[20] A. Tanwar, H. A. Gandhi, D. Kushwaha, and J. Bhattacharya, “A review on microelectrode array fabrication techniques and their applications,” *Materials Today Chemistry*, vol. 26, p. 101153, Dec. 2022, doi: 10.1016/j.mtchem.2022.101153.

[21] B. D. Gates, Q. Xu, J. C. Love, D. B. Wolfe, and G. M. Whitesides, “UNCONVENTIONAL NANOFABRICATION,” *Annu. Rev. Mater. Res.*, vol. 34, no. 1, pp. 339–372, Aug. 2004, doi: 10.1146/annurev.matsci.34.052803.091100.

[22] M. J. Madou, *Manufacturing Techniques for Microfabrication and Nanotechnology*, 3rd ed. Boca Raton: Taylor & Francis Group, 2011.

[23] P. Rai-Choudhury, *Handbook of Microlithography, Micromachining, and Microfabrication. Volume 1: Microlithography*. SPIE PRESS, 1997. doi: 10.1117/3.2265070.

[24] F. Burmeister, S. Steenhusen, R. Houbertz, U. D. Zeitner, S. Nolte, and A. Tünnermann, “Materials and technologies for fabrication of three-dimensional microstructures with sub-100 nm feature sizes by two-photon polymerization,” *Journal of Laser Applications*, vol. 24, no. 4, p. 042014, Sep. 2012, doi: 10.2351/1.4730807.

[25] W. Kaiser and C. G. B. Garrett, “Two-Photon Excitation in Ca F 2 : Eu 2 +,” *Phys. Rev. Lett.*, vol. 7, no. 6, pp. 229–231, Sep. 1961, doi: 10.1103/PhysRevLett.7.229.

[26] S. O’Halloran, A. Pandit, A. Heise, and A. Kellett, “Two-Photon Polymerization: Fundamentals, Materials, and Chemical Modification Strategies,” *Advanced Science*, vol. 10, no. 7, p. 2204072, Mar. 2023, doi: 10.1002/advs.202204072.

[27] V. Harinarayana and Y. C. Shin, “Two-photon lithography for three-dimensional fabrication in micro/nanoscale regime: A comprehensive review,” *Optics & Laser Technology*, vol. 142, p. 107180, Oct. 2021, doi: 10.1016/j.optlastec.2021.107180.

[28] A. Brenner and G. E. Riddell, “Nickel plating on steel by chemical reduction,” *J. RES. NATL. BUR. STAN.*, vol. 37, no. 1, p. 31, Jul. 1946, doi: 10.6028/jres.037.019.

[29] C. A. Deckert, “Electroless Copper Plating A Review: Part I,” 1995.

[30] F. Hanna, Z. A. Hamid, and A. A. Aal, “Controlling factors affecting the stability and rate of electroless copper plating,” *Materials Letters*, vol. 58, no. 1–2, pp. 104–109, Jan. 2004, doi: 10.1016/S0167-577X(03)00424-5.

[31] C. F. Coombs and H. T. Holden, Eds., *Printed circuits handbook*, Seventh edition. in McGraw-Hill handbooks. New York Chicago San Francisco Athens London Madrid Mexico City Milan New Delhi Singapore Sydney Toronto: McGraw-Hill, 2016.

[32] S. van Kesteren, “Active, adaptive, and replicating coloidal clusters”.

[33] L. Pertoldi, V. Zega, C. Comi, and R. Osellame, “Dynamic mechanical characterization of two-photon-polymerized SZ2080 photoresist,” *Journal of Applied Physics*, vol. 128, no. 17, p. 175102, Nov. 2020, doi: 10.1063/5.0022367.

[34] N. G. Van Kampen, “THE LANGEVIN APPROACH,” in *Stochastic Processes in Physics and Chemistry*, Elsevier, 2007, pp. 219–243. doi: 10.1016/B978-044452965-7/50012-X.

[35] R. N. Bracewell, *The Fourier transform and its applications*, 3rd ed. in McGraw-Hill series in electrical and computer engineering. Boston: McGraw Hill, 2000.

4 Appendix – Derivations and images

The goal of the following section is to summarize the evolution and relevance of the Langevin equations and Boltzmann distributions. This is relevant to understanding the experimental system as applied to the calculation and quantification of various physical constants such as effective temperature, T_{eff}, resonance frequency, ω_0, damping coefficient, γ, and spring constant, k. We focus on four derivations: spring constant, positional distribution, velocity distribution and Power Spectral Density (PSD). This chapter draws heavily from Alan V. Oppenheim's, *Signals and Processes* [10], Daniel Kleppner's, *An Introduction to Mechanics* [12], N. G. Van Kampen's, *Stochastic Processes in Physics and Chemistry (The Langevin Approach)* [34] and Ronald N. Bracewell's, *The Fourier transform and its applications* [35].

A. Spring constant as a function of systematic geometry

Starting with the gravitational potential energy, $U(x)$, as a function of x:

$$U(x) = mgh(x)$$

With height $h(x)$ expressed as a function of the surface curvature (radius of curvature = r),

$$h(x) = r\sqrt{1 - \left(\frac{x}{r}\right)^2}$$

For small displacements near equilibrium i.e., near $x = 0$, and $x \ll r$, we expand the Taylor series around $x = 0$. First, expressing $h(x)$,

$$h(x) = r\left(1 - \frac{x^2}{r^2}\right)^{\frac{1}{2}}$$

Applying the binomial expansion for $(1 - z)^n$ for when z is small,

$$(1 - z)^n \approx 1 + nz + \frac{n(n-1)}{2}z^2 + \cdots$$

For small x, $\frac{x^2}{r^2} \ll 1$, so we use the binomial expansion for $(1 - z)^{\frac{1}{2}}$ where $z = \frac{x^2}{r^2}$ and $n = \frac{1}{2}$

$$(1 - z)^{\frac{1}{2}} \approx 1 - \frac{z}{2}$$

Substituting $z = \frac{x^2}{r^2}$

$$\left(1 - \frac{x^2}{r^2}\right)^{\frac{1}{2}} \approx 1 - \frac{1}{2}\frac{x^2}{r^2}$$

$$h(x) \approx r - \frac{x^2}{2r}$$

Substituting into the potential energy, $U(x)$,

$$U(x) = mg(r - \frac{x^2}{2r})$$

Considering the standard expression for harmonic potential energy,

$$U(x) = mgh(x) = \frac{1}{2}kx^2$$

This reduces to

$$k = \frac{mg}{r} \tag{1.2.3}$$

B. Position distribution

Consider our system (in one dimension) that obeys the Langevin equation presented in Section 1.1.1, with energy, E, dominated by the force due to a harmonic oscillator:

$$E = \frac{1}{2}kx^2$$

where k is the spring constant, and the Boltzmann equation is:

$$P(E) \propto e^{\frac{-E}{k_B T}}$$

$$P(x) = N\, e^{\frac{-kx^2}{2k_B T}}$$

Summing over all energy states:

$$1 = N \int_{-\infty}^{\infty} e^{\frac{-kx^2}{2k_B T}}$$

$$N = \sqrt{\frac{2\pi k_B T}{k}}$$

$$P(x) = \sqrt{\frac{k}{2\pi k_B T}}\, e^{\frac{-kx^2}{2k_B T}}$$

But,

$$\sigma^2 = \frac{k_B T}{k}$$

$$P(x) = \frac{1}{\sqrt{2\pi\sigma^2}} e^{\frac{x^2}{2\sigma^2}} \tag{1.3.1}$$

C. Velocity distribution

Consider our system (in one dimension) that obeys the Langevin equation presented in Section 1.1.1, with energy, E, whose velocity is dominated by the kinetic energy due to the vibrations:

$$E = \frac{1}{2} m {v_x}^2$$

where k is the spring constant, and the Boltzmann equation is:

$$P(E) \propto e^{\frac{-E}{k_B T}}$$

$$P(V_x) = N\, e^{\frac{-mv_x^2}{2k_B T}}$$

Summing over all energy states:

$$1 = A \int_{-\infty}^{\infty} e^{\frac{-m{v_x}^2}{2k_B T}}$$

$$A = \sqrt{\frac{2\pi k_B T}{m}}$$

$$P(V_x) = \sqrt{\frac{m}{2\pi k_B T}}\, e^{\frac{-mv^2}{2k_B T}} \tag{1.3.3}$$

D. Power Spectral density

Consider the Langevin equation:

$$m\frac{d\mathbf{v}}{dt} = -\gamma\mathbf{v} - kx + \eta(t)$$

Rewritten as:

$$m\ddot{x}(t) + -\gamma\dot{x}(t) + kx(t) = \eta(t)$$

Fast Fourier Transform (FFT) of the Langevin:

$$m(-\omega^2)\chi(\omega) + \gamma(i\omega)\chi(\omega) + k\,\chi(\omega) = \eta(\omega)$$

$$\chi(\omega)[m(-\omega^2) + \gamma(i\omega) + k] = \eta(\omega)$$

$$\chi(\omega) = \frac{\eta(\omega)}{-m\omega^2 + i\gamma\omega + k}$$

But PSD of *x*,

$$S_{xx}(\omega) = \langle\, |\chi(\omega)|^2 \,\rangle$$

$$S_{xx}(\omega) = \langle \left|\frac{\eta(\omega)}{-m\omega^2 + i\gamma\omega + k}\right|^2 \rangle$$

In the frequency domain,

$$\langle\, |\eta(\omega)|^2 \,\rangle = 2k_B T\gamma$$

Since the denominator is a complex number $(-m\omega^2 + k) + i\gamma\omega$, the squared magnitude simplifies to:

$$|(-m\omega^2 + k) + i\gamma\omega|^2 = (m\omega^2 - k)^2 + \gamma^2\omega^2$$

Introducing the resonance frequency:

$$\omega_0 = \sqrt{\frac{k}{m}} \qquad (1.2.4)$$

The PSD therefore convolves to:

$$S_{xx}(\omega) = \frac{2K_B T\,\gamma}{m[(\omega^2 - \omega_0^2)^2 + \gamma^2\omega^2]} \qquad (1.1.5)$$

E. Correlation functions at different time scales

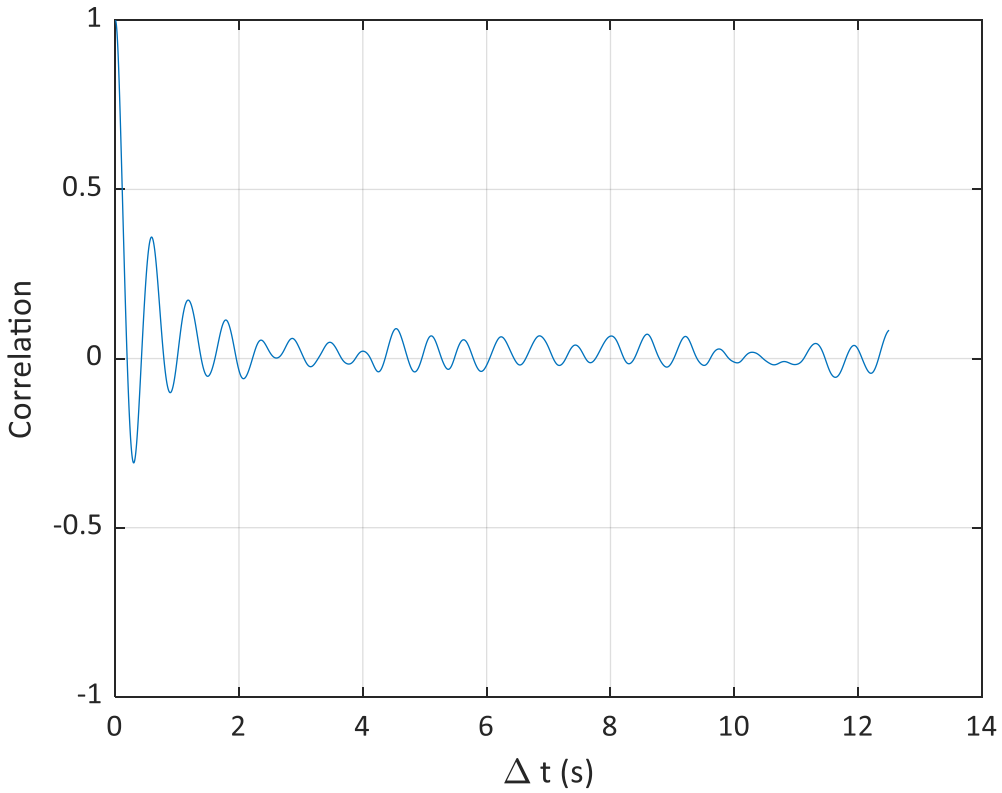

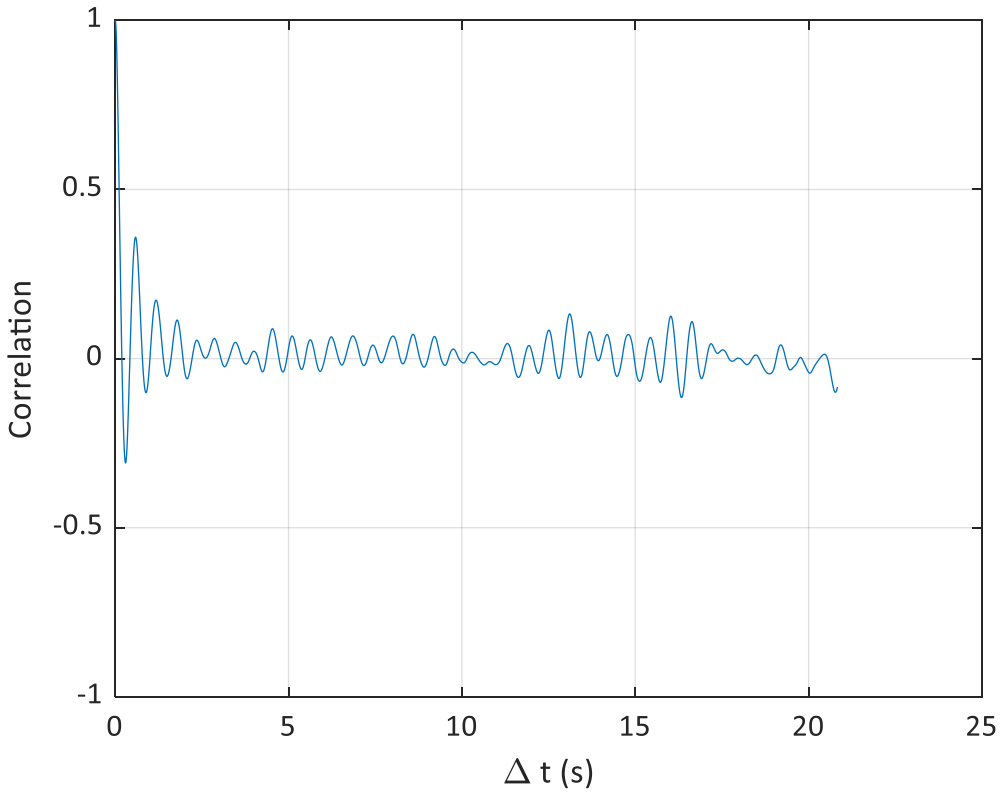

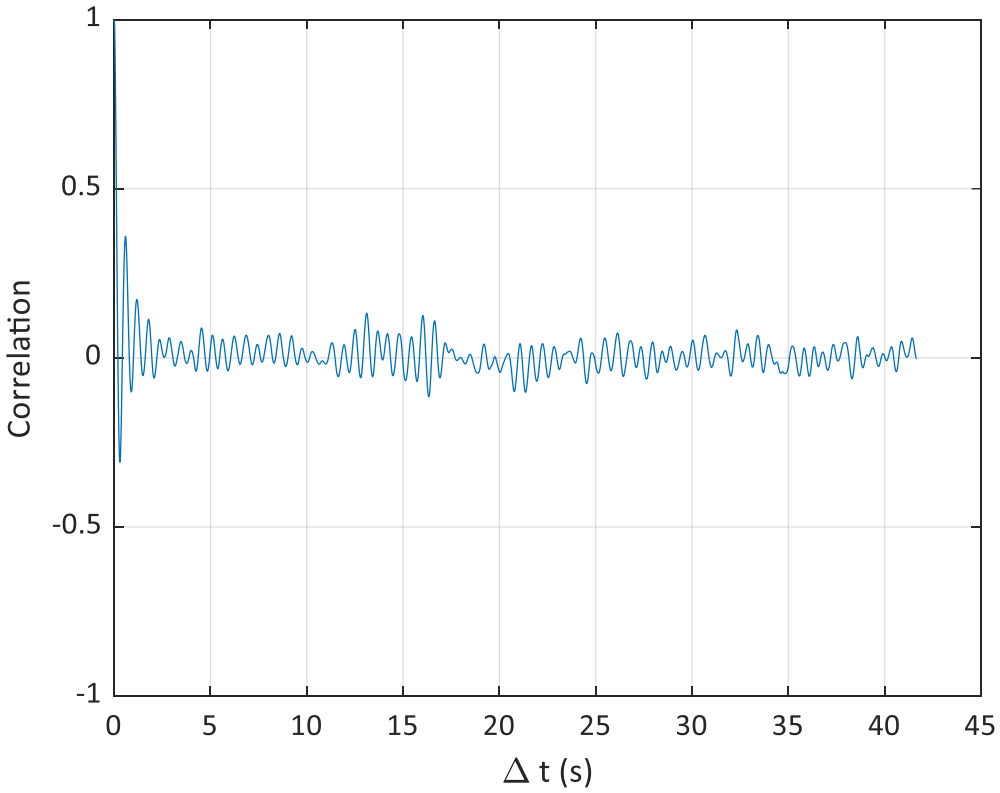

F. STL images of printed structures with micrometer scale bars

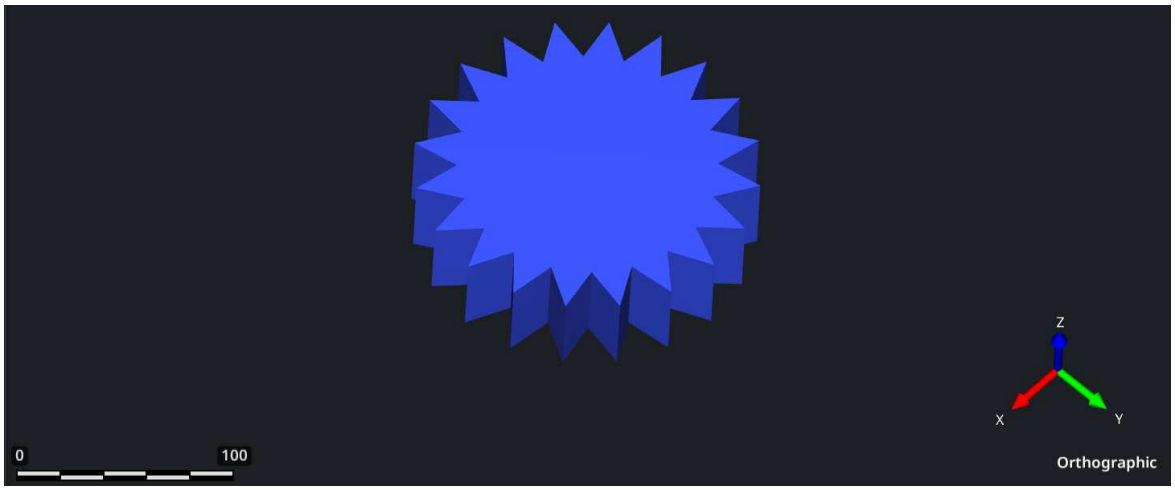

***Figure F.1**. 20-point gear*

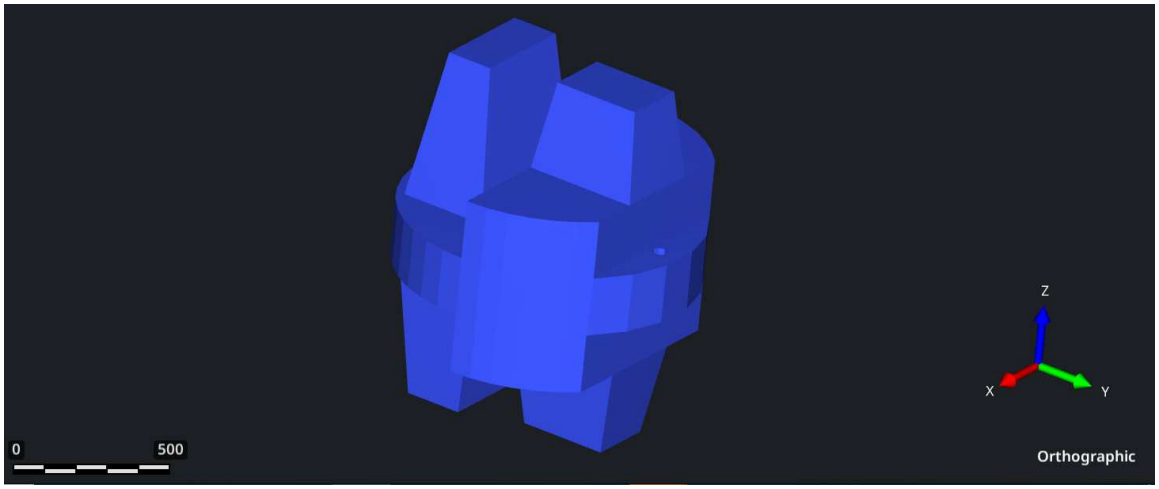

Figure F.2. *Asymmetrical particle*

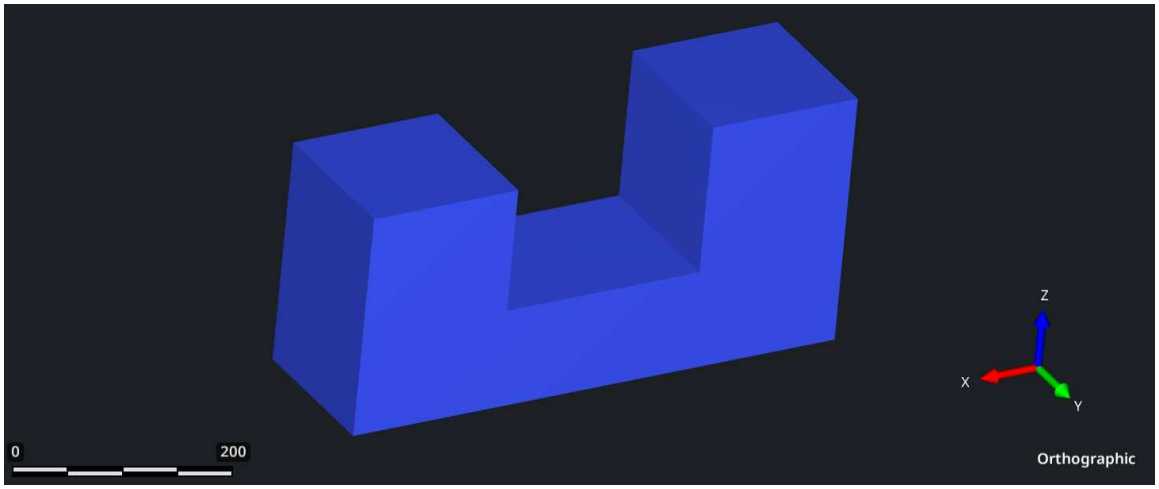

Figure F.3. *Walker*

Figure F.4. *Asymmetrical particle*

***Figure F.5**. Micrometric beam*

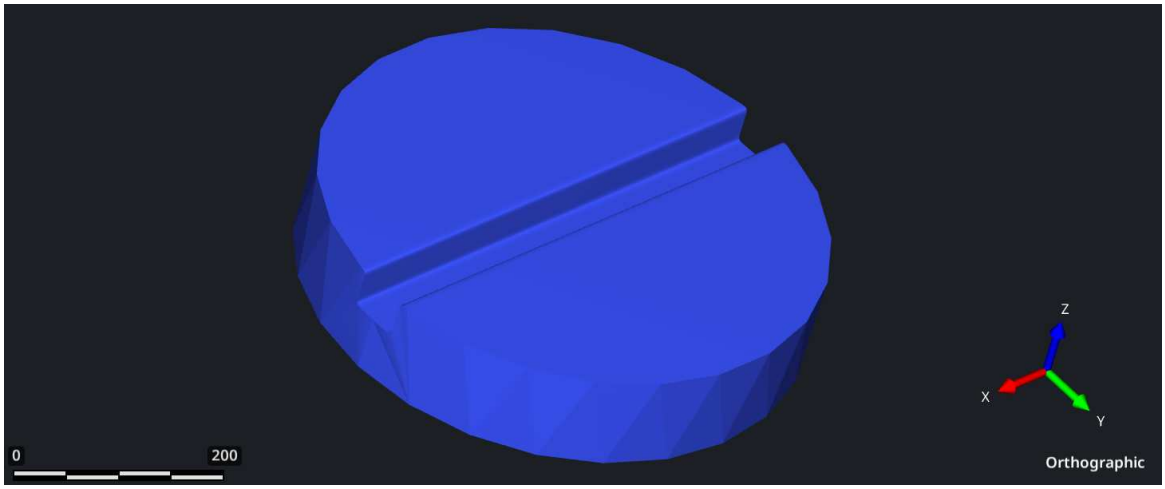

***Figure F.6.** Puck*

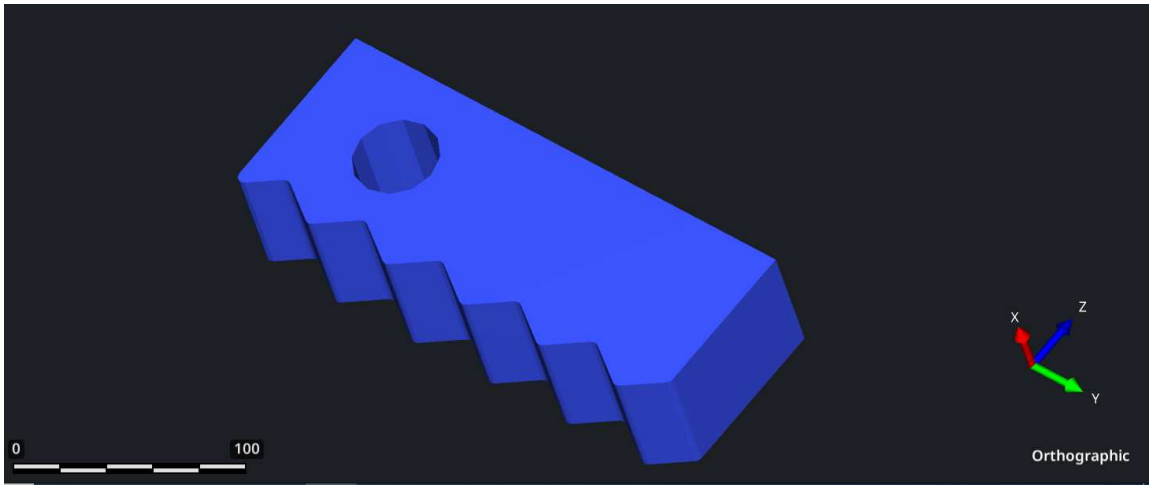

***Figure F.7.** Teeth*

G. Structure imaging and characterization

The images presented in this thesis were captured by field-emission scanning electron microscopy (FE-SEM), confocal microscopy and brightfield optical microscopy. The bright-field optical microscopy images were taken using a Nikon Eclipse Ti optical microscope at various magnifications. The objectives used were a 40X Nikon S FLUOR objective, NA 0.6 and a 4X Nikon Plan Fluor objective, NA 0.13.

The SEM images were taken using a Merlin Compact VP Carl Zeiss FE-SEM with a HeSe detector, at an EHT voltage of 3kV.

Confocal microscopy images are captured using a Nikon Eclipse Ti2 microscope equipped with a Nikon Plan APO 40x objective (NA = 0.95, WD = 250um), Crest Optics X-Light V3 spinning disk, Lumencore Celesta light source, and Teledyne Photometrics Prime 95B camera. All fluorescent images are excited using 488nm light and emission is captured at 511nm.

All AFM measurements were performed on a NX20 instrument (Park Systems, South Korea) with pre mounted cantilever probes (PPP-NCHR, Park Systems, South Korea) with a spring constant of 42 Nm^{-1} and resonance frequency of 400 kHz. AFM topography measurements were conducted in non-contact mode at a scanning rate of 0.3 Hz. Young's modulus measurements were conducted in contact mode at a scanning rate of 89.7×10^{-3} Hz and a set point of 6.5 nN. Before obtaining the force-distance curve a force slope correction, A-B sensitivity calibration of the PSPD and a spring constant calibration of the cantilever were performed. A Hertzian model was used to calculate the Young's modulus.

H. Diffusive behavior

Characteristic	**Power law exponent, $\propto$**	**Equation**	**Description**
Ballistic	$\alpha = 2$	$\langle x^2(t)\rangle \sim t^2$	Straight line, directed motion
Super diffusive	$1 < \alpha < 2$	$\langle x^2(t)\rangle \sim t^{\propto}$	Faster-than-diffusion spread
Diffusive	$\alpha = 1$	$\langle x^2(t)\rangle \sim t$	Normal, Brownian motion
Sub diffusive	$0 < \alpha < 1$	$\langle x^2(t)\rangle \sim t^{\propto}$	Slower-than-diffusion, hindered motion